Unsteady granular chute flows at high inertial numbers

Satyabrata Patro● and Anurag Tripathi ●[*]
Department of Chemical Engineering, Indian Institute of Technology Kanpur, Uttar Pradesh 208016, India

Sumit Kumar
Dr. Reddy's Laboratories Ltd., Hyderabad, Telangana 500090, India

Anubhav Majumdar ●
Oracle, Bengaluru, Karnataka 560076, India

We study the time-dependent flow behavior of gravity-driven free surface granular flows using the discrete element method and continuum modeling. Discrete element method (DEM) simulations of slightly polydisperse disks flowing over a periodic chute with a bumpy base are performed. A simple numerical solution based on a continuum approach with the inertial-number-based μ-I rheology has been proposed to predict the flow dynamics. The results of the continuum model are compared with the DEM simulation results for a wide range of chute inclinations. Solutions for the constitutive model described by the popular Jop-Forterre-Pouliquen (JFP) model as well as the recently proposed modified rheological model using a nonmonotonic variation of μ-I are obtained. Our results demonstrate that the popular JFP model reliably predicts the flow at low to moderate inclination angles (i.e., for $I \lesssim 0.5$). However, it fails to predict the flow properties at high inclinations. The modified rheological model, on the other hand, is very well able to predict the time-averaged flow properties for all the inclination angles considered in this study. Accounting for the presence of the slip velocity, layer dilation, and stress anisotropy is found to be crucial for accurate predictions of transient flows at high inertial numbers (i.e., for $I \gtrsim 1$).

I. INTRODUCTION

The rheology of granular materials has been an active research topic for the last few decades due to its wide occurrence in geophysical as well as industrial situations. A number of experimental [1–18] as well as simulation studies using the discrete element method (DEM) [2,19–33] have been utilized to explore the rheology of granular materials. A detailed review of granular flow rheology in different configurations can be found in Refs. [34–36]. These studies have shown that the granular flow between the two limiting cases of quasistatic slow flows, and rapid dilute flows is controlled by a nondimensional inertial number $I = d\dot{\gamma}/\sqrt{P/\rho_p}$, which depends on the local shear rate $\dot{\gamma}$ and pressure P in addition to the particle size d and density ρ_p. This intermediate dense flow regime has been studied in a variety of configurations. The inertial number-based rheological description for this dense flow regime has been confirmed in chute flows [2,19,24,32,37], plane shear flows [2,20,27,29], annular shear cells [13], granular collapse [8–10,38], planar silos [30,31],

---

*anuragt@iitk.ac.in

heap flows [3], and rotating cylinders [16,39]. Both experiments as well as simulations confirm that the ratio of the shear stress to the pressure depends on the inertial number in this regime. The most popular model for the inertial-number-based rheology is the Jop-Forterre-Pouliquen (JFP) model [37].

According to this model, the ratio of the shear stress τ_{yx} to the pressure P, termed as the effective friction coefficient $\mu = |\tau|/P$, varies in a nonlinear fashion with I. Starting from a minimum effective friction coefficient μ_s at $I \sim 0$, μ increases with I. The inertial-number-based JFP model [37] has been able to capture the flow behavior of granular materials in experiments [2,3,40] as well as simulations [19,20,41] in the dense flow regime for inertial number $I \leqslant 0.6$. In the absence of simulation and experimental data at large I values, the model assumes that the effective friction coefficient μ at large inertial numbers becomes constant. In addition, the solids fraction also decreases with the inertial number. The solids fraction ϕ is defined as $\phi = V_p/V$, where V_p is the total volume of the particles in a region of volume V. Accounting for the solids fraction variation in the continuum simulations requires the incorporation of compressibility effects. In order to use the commonly employed approach for incompressible fluid flows, most studies ignore the density variation in the continuum simulation of granular flows. The incompressible JFP model has been used to predict the steady-state flow properties in chute flows [4,37,38,42–46], vertical chutes [46], and steady plane shear [45], as well as flow through an annular shear cell [42,47]. The incompressible μ-I model or its variants have also been used to predict the transient flow of granular materials flowing over a chute [43–45,48–51], material discharging from granular silos [42,49,52,53], and flow during column collapse [38,45,49,50,54], in addition to rotating drums [44] and heap flows [46].

The time-dependent response of granular media in bounded heap flow has been studied using DEM simulations and experiments [55]. Efforts have also been made to capture the experimentally observed transient behavior of granular slides in air as well as water [56]. The depth-averaged model approach has also been utilized in the past to predict the flow behavior of granular materials over a chute [57–60]. Granular flows also exhibit some nonlocal effects during slow flows such as shear banding, weak dependence of stress on the magnitude of shear rate, and dilation effects [61]. Some nonlocal continuum models have also been proposed to understand the flow behavior of granular materials [47,62–64]. Recently Debnath *et al.* [65] solved and compared different compressible μ-I [66,67] as well as nonlocal rheological models [47,61] with the DEM simulations of flow in a vertical chute. These models are found to have limited success in predicting the flow properties. A review of the nonlocal modeling for granular flows is presented in Ref. [68]. Concerns about studies dealing with time-dependent continuum simulations have been raised in the past. Barker *et al.* [48] showed that the incompressible JFP model is well posed only for a narrow range of inertial numbers; for very low and relatively high values of inertial numbers, it is found to be ill posed. A wider range of well-posed regions can be obtained by partial regularization of the μ-I model by deriving a new functional form of the μ-I model so that the granular material no longer has yield stress [43]. The compressible rheology has been implemented to understand the behavior of subaqueous granular collapse [54]. Few efforts have also been made to introduce bulk compressibility effects [66,67,69] to regularize the μ-I model. Recently Barker *et al.* [44] implemented the regularized well-posed μ-I rheology [43] intercoupled with segregation in a continuum framework to capture the qualitative behavior of flow evolution and segregation of multicomponent mixtures in an inclined plane and rotating tumbler.

All of the aforementioned studies using inertial number rheology employ the assumption that the effective friction coefficient becomes constant at high inertial numbers. Mandal and Khakhar [27,29], however, in their simulation study of the flow of dumbbells in plane shear flows, showed that the saturating behavior of the effective friction coefficient μ at higher inertial number I used in such studies is not correct. Instead, μ is found to decrease with I after achieving a maximum. However, the authors were unable to observe similar behavior in the case of chute flows. A recent study by Patro *et al.* [32] has shown that the nonmonotonic variation of the effective friction coefficient μ with the inertial number I is observed in the case of chute flows as well. Figure 1(a) shows
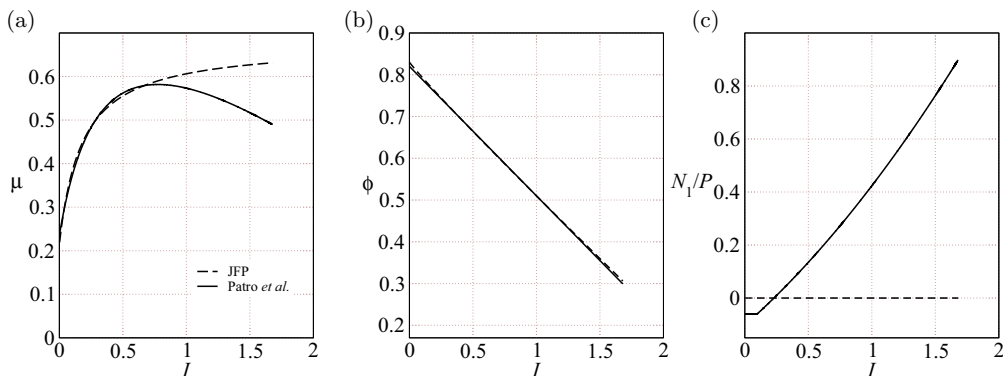
FIG. 1. Variation of the (a) effective friction coefficient μ with the inertial number I, (b) solids fraction ϕ with I, and (c) ratio of normal stress difference to the pressure, N_1/P, with I using the model parameters from Patro *et al.* [32]. Solid lines represent the variation according to the modified rheology. The dashed line represents the fitted line using the JFP model.

the variation of the effective friction coefficient with the inertial number (solid line) as suggested by the modified rheology of Patro *et al.* [32]. The broken line shows the variation according to the JFP model. Figure 1(b) shows the variation of the solids fraction ϕ with the inertial number I for the two models. Figure 1(c) shows the variation of the ratio of the normal stress difference to the pressure, N_1/P, with the inertial number I. Note that the JFP model does not account for the presence of normal stress difference and hence $N_1 = 0$ at all inertial numbers. Nonzero normal stress differences in granular flows, however, have been observed by other researchers [70–74]. By accounting for the normal stress difference law in the modified rheological model, Patro *et al.* [32] also confirmed that two different flow states at the same inclination angle of the chute are not possible despite the nonmonotonic variation of μ with I. The authors also showed that the modified rheological description coupled with momentum balance equations is able to predict various flow properties of interest at steady state for chute flow of disks at different inclination angles. These predictions have been found to be in good agreement with DEM simulation results for periodic chute flows even at high inertial numbers. However, predictions for time-dependent properties for high-inertial-number granular flows have not been compared with DEM simulations to the best of our knowledge.

In this study, we focus on unsteady granular flows down an inclined surface in a periodic chute flow configuration spanning a large range of inclination angles to cover a wide range of inertial numbers. Parez *et al.* [51] obtained analytical expressions by solving the momentum balance equation coupled with a linear μ-I relation for such a system. Extending this analytical approach to the nonlinear μ-I rheological model is much more complex and mathematically challenging. Hence, we solve the resulting equation numerically to predict the time-dependent flow properties. The predictions obtained from the numerical solution are compared with the DEM simulation results for inertial numbers close to or greater than unity. Our results show that using the JFP model at high-inertial-number flows leads to significant overprediction of the average velocity along with underprediction of solids fraction.

The organization of the paper is as follows. The DEM simulation methodology is briefly mentioned in Sec. II. The theoretical formulation as well as the numerical technique used to solve the resulting equation are described in Sec. III. Results obtained from the numerical solution of the momentum balance equation are compared with the DEM simulations in Sec. IV. Discussion about some important observations is reported in Sec. V. Summary and future work are presented in Sec. VI.
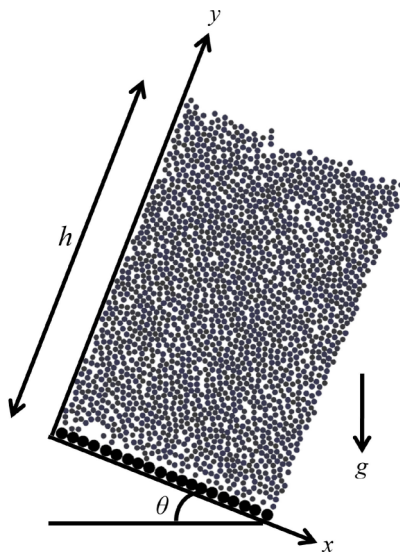
FIG. 2. Snapshot of simulation of a granular layer flowing under the influence of gravity at an inclination $\theta = 32°$ from the horizontal at any instant. Solid black circles represent the static particles that form the bumpy chute base and solid grey circles represent the flowing disks.

II. SIMULATION METHODOLOGY

The DEM technique is used to simulate slightly polydisperse ($\pm 5\%$ polydispersity), inelastic, frictional disks flowing over a rough and bumpy inclined surface. A schematic of the simulation setup is shown in Fig. 2. The length of the simulation box is $40d$, where d is the mean diameter of the disks. To mimic an infinite length of the chute, a periodic boundary condition is imposed in the flowing (x) direction. The base of the simulation domain consists of static bumpy particles of size $2d$ to reduce the slip at the base. The contact force between the disks is modeled using the linear spring and dashpot model as in the L2 model of Silbert *et al.* [19]. The coefficient of static friction, μ, is chosen as 0.5 and two different values of the normal restitution coefficient ($e_n = 0.5$ and 0.1) are considered. The initial arrangement of the particles is done on a square lattice with a finite spacing between the surface of particles and they are given small random initial velocities. In order to simulate the flow of particles from rest, the particles are allowed to settle under the influence of gravity until the average kinetic energy of the particles in the layer becomes less than $10^{-6}mgd$. The height of the settled layer of $N = 2000$ particles following this protocol is $h \sim 50d$. At time $t = 0$, the direction of the gravity is changed to the desired inclination angle θ. The flow is allowed to evolve until the average kinetic energy of the system of particles becomes constant, indicating that the system has achieved a steady state. To compute the flow properties, the simulation domain is divided into a number of strips in the y direction. The thickness of each strip is equal to the mean particle diameter d so that the reported properties are averaged over the strip area $A = L_x \times d$. The properties reported at any instant t are averaged over 60 snapshots having an interval of 0.1 time unit between successive snapshots and thus represent the average property over the last six time units. The partial contribution of the particle's area in each strip is accounted for while calculating various flow profiles such as velocity, solids fraction, stresses, etc. Unless stated otherwise, the results are reported in dimensionless form using d as the length scale, m as the mass scale, $\sqrt{d/g}$ as the timescale, gd as the velocity scale, mg as the force scale, and mgd as the energy scale. More details are available in Ref. [32].

III. THEORY

Consider a fully developed granular flow over a surface inclined at an angle θ under the influence of gravity. Assuming a unidirectional flow in the x direction, the momentum balance equation in x and y directions simplifies to

$$\rho_b \frac{\partial v_x}{\partial t} = -\frac{\partial \tau_{yx}}{\partial y} + \rho_b g \sin \theta, \tag{1}$$

$$0 = -\frac{\partial \sigma_{yy}}{\partial y} - \rho_b g \cos \theta, \tag{2}$$

where v_x is the velocity along the flow direction, θ is the inclination angle, τ_{yx} is the shear stress, g is the gravitational acceleration, and $\rho_b = \phi(y)\rho_p$ is the bulk density of the medium with ρ_p being the density of the particle and $\phi(y)$ is the local solids fraction at any y. Integrating Eq. (2) with y, we get

$$\sigma_{yy} = \rho_p g \cos \theta \int_y^h \phi(y) dy. \tag{3}$$

Assuming the variation of $\phi(y)$ along y at any instant to be small, we approximate the integral in Eq. (3) as $\int_y^h \phi(y)dy = \phi_{\text{avg}}(h - y)$, so that the expression for σ_{yy} simplifies to

$$\sigma_{yy} = \rho_p g \cos \theta \phi_{\text{avg}}(h - y). \tag{4}$$

According to the μ-I rheology, the flow behavior depends upon the nondimensional inertial number I defined as

$$I = \frac{|\dot{\gamma}|d}{\sqrt{P/\rho_p}}. \tag{5}$$

For the case of unidirectional chute flow, the second invariant of the strain rate tensor $|\dot{\gamma}|$ equals the shear rate dv_x/dy, i.e., $|\dot{\gamma}| = dv_x/dy$. The effective friction coefficient $\mu(I)$ is defined as the ratio of the second invariant of the stress tensor $|\tau_{yx}|$ to the pressure P, i.e.,

$$\mu(I) = \frac{|\tau_{yx}|}{P}. \tag{6}$$

The JFP model uses the following form to relate the effective friction coefficient $\mu(I)$ with I:

$$\mu(I) = \mu_s' + \frac{\mu_m' - \mu_s'}{1 + I_0'/I}, \tag{7}$$

with μ_s', μ_m', and I_0' being the model parameters. Our recent study [32] shows that a more appropriate variation of $\mu(I)$ is given by

$$\mu(I) = \mu_s + \frac{c_1 - c_2 I}{1 + I_0/I}. \tag{8}$$

The proposed rheology is complemented with an empirical relation to describe the variation of solid fraction (ϕ) with inertial number I as

$$\phi = \phi_{\text{max}} - aI^\alpha, \tag{9}$$

where ϕ_{max}, a, and α are the model parameters [32]. Some studies [75] indicate that the volume fraction needs some minimum deformation (or strain) to relax to its steady-state value during the transient evolution in the case of suspensions and the early response of the suspension is not by the steady-state rheology. Given the absence of any fluid effect in our simulations, we ignore such effects and assume that the solids fraction adapts to its equilibrium value instantaneously using Eq. (9). In addition, we find that the role of the normal stress difference becomes important at high inclinations. This presence of the normal stress difference is accounted by a normal stress

difference law in the rheology by proposing the ratio of the first normal difference $N_1 = \sigma_{xx} - \sigma_{yy}$ to the pressure $P = (\sigma_{xx} + \sigma_{yy})/2$ as a function of inertial number I, i.e.,

$$\frac{N_1}{P} = f(I). \tag{10}$$

Using Eqs. (4), (6), and (10) we get the expression for pressure as

$$P = \frac{\phi_{\text{avg}} \rho_p g \cos\theta (h - y)}{1 - 0.5 f(I)}. \tag{11}$$

As expected, in the absence of normal stress difference, the expression for pressure reduces to a hydrostatic head. A recent study by Patro *et al.* [32] shows that $f(I)$ remains constant up to $I \leqslant I^*$ and varies quadratically with inertial number I for $I > I^*(= 0.1)$, i.e.,

$$f(I) = \begin{cases} k & \text{for } I \leqslant 0.1 \\ AI^2 + BI + C & \text{for } I > 0.1. \end{cases} \tag{12a}$$
$$\tag{12b}$$

Using the expression of pressure P from Eq. (11) in Eq. (5), we get

$$I = \frac{|\dot{\gamma}| d \sqrt{1 - 0.5 f(I)}}{\sqrt{g \cos\theta (h - y) \phi_{\text{avg}}}}. \tag{13}$$

Equation (13) can be rearranged to get the expression for I as follows:

$$I = \begin{cases} \frac{-B_0 + \sqrt{B_0^2 - 4A_0 C_0}}{2A_0} & \text{for } I > 0.1 \\ \frac{|\dot{\gamma}| d \sqrt{1 - 0.5k}}{\sqrt{g \cos\theta (h - y) \phi_{\text{avg}}}} & \text{for } I \leqslant 0.1, \end{cases} \tag{14a}$$
$$\tag{14b}$$

with $A_0 = g \cos\theta (h - y) \phi_{\text{avg}} + 0.5A|\dot{\gamma}|^2 d^2$, $B_0 = 0.5B|\dot{\gamma}|^2 d^2$, and $C_0 = (0.5C - 1)|\dot{\gamma}|^2 d^2$. The calculated inertial number is used in the empirical form relating the effective friction coefficient $\mu(I)$ with the inertial number I. Equations (7) and (8) show two such empirical forms that can be utilized to obtain the time-dependent properties of the flow. Using Eqs. (6) and (11), we get

$$\tau_{yx} = \mu(I) \left(\frac{\phi_{\text{avg}} \rho_p g \cos\theta (h - y)}{1 - 0.5 f(I)} \right). \tag{15}$$

Differentiating Eq. (17) with respect to y and substituting $\frac{\partial \tau_{yx}}{\partial y}$ in Eq. (1), we get

$$\phi(I) \frac{\partial v_x}{\partial t} = \phi(I) g \sin\theta - \frac{\partial}{\partial y} \left[\mu(I) \phi_{\text{avg}} \left(\frac{\rho_p g \cos\theta (h - y)}{1 - 0.5 f(I)} \right) \right]. \tag{16}$$

In writing Eq. (16), we account for the variation of ϕ with y in the x momentum balance equation. However, in the calculation of σ_{yy}, the variation of ϕ with y is ignored and $\phi(y)$ is replaced by the average value ϕ_{avg} [Eq. (4)]. We also solve Eq. (16) by accounting for the variation of ϕ along y in the calculation of σ_{yy} using Eq. (3). We find that the results obtained are not altered significantly due to this more refined calculation of the σ_{yy}. Hence we use Eq. (4) for the calculation of σ_{yy} in all the results presented in this work. In order to solve Eq. (16), we use the PDEPE solver in MATLAB along with the following initial conditions (ICs) and boundary conditions (BCs):

$$\text{IC: } v_x(y, 0) = 0, \tag{17a}$$

$$\text{BC1: } \tau_{yx}(h, t) = 0, \tag{17b}$$

$$\text{BC2: } v_x(0, t) = v_{\text{slip}}(t). \tag{17c}$$

The initial condition [Eq. (17a)] represents that the velocity across the layer at $t = 0$ is zero and mimics the flow starting from rest. The first boundary condition [Eq. (17b)] corresponds to zero shear stress at the free surface $y = h$. The second boundary condition [Eq. (17c)] corresponds to a

known slip velocity at the base. While a no-slip boundary condition seems to be appropriate for low inclinations, this boundary condition is needed to account for the sufficient slip observed at high inclinations [32]. The general form of the partial differential equation used by the PDEPE solver in MATLAB is given as follows:

$$c\left(y, t, u, \frac{\partial u}{\partial y}\right)\frac{\partial u}{\partial t} = y^{-m}\frac{\partial}{\partial y}\left(y^m F\left(y, t, u, \frac{\partial u}{\partial y}\right)\right) + s\left(y, t, u, \frac{\partial u}{\partial y}\right). \tag{18}$$

Equation (16) can be written in the above general form using $u = v_x$ and $c = \phi(I)$, $m = 0$, $s = \phi(I)g\sin\theta$, and $F = \mu(I)\phi(I)(\frac{\rho_p g\cos\theta(h-y)}{1-0.5f(I)})$.

The PDEPE solver represents the derivatives numerically by discretizing the domain into finite spatial and temporal grids. The number of grids along the y direction is chosen to be $N = 50$ and the time step Δt is chosen to be 0.1. Equation (9), which is referred to as the dilatancy law, dictates that the solids fraction ϕ of the medium decreases with an increase in the inertial number. With increasing velocity (and hence inertial number), the flowing granular layer dilates and leads to an increase in the layer thickness h with time t. Our DEM simulation results show that this increase in the layer height becomes very significant at high inertial numbers. This significant dilation of the granular layer indicates that the compressibility effects become important at high inertial numbers and need to be accounted for by solving the continuity equation as well. Given our assumption of the unidirectional flow, the y component of the velocity is ignored in our theoretical formulation. For this reason, accounting for the variation of ϕ with t is not possible using the equation of continuity. We circumvent this problem by using the integral mass balance equation. Since our simulation method utilizes a periodic simulation box with a fixed mass of particles, we account for the height of the layer at any instant by equating the mass at time t to the mass in the beginning of the simulation. The height of the layer is $h_{t=0} = h_{\min}$ at $t = 0$ as it starts from rest with the maximum solids fraction $\phi_{t=0} = \phi_{\max}$ across the entire layer. The mass per unit width of the flowing layer of the disks at any time instant t is equal to $\int_0^{h(t)}\rho_b(t)dy$. Using $\rho_b(t) = \phi(t)\rho_p$ and equating the mass at any instant to the initial mass of the layer, we get $\int_0^{h(t)}\phi(t)dy = h_{\min}\phi_{\max}$. Since $\int_0^{h(t)}\phi(t)dy = h(t)\phi_{\text{avg}}(t)$, the height at any instant can be obtained using $h(t) = \frac{h_{\min}\phi_{\max}}{\phi_{\text{avg}}(t)}$, where $\phi_{\text{avg}}(t)$ is the average solids fraction across the layer at any instant t. The detailed steps for computing the time-dependent properties of the flowing layer are given in Algorithm 1.

IV. RESULTS

In this section, we present results for the time-dependent flow of disks over an inclined surface using DEM simulations and compare them with the theoretical predictions. The results are reported in dimensionless form for two different restitution coefficients $e_n = 0.5$ and $e_n = 0.1$. The theoretical predictions are obtained by solving the momentum balance equations along with the inertial-number-based JFP model popularly used for describing the behavior of dense granular flows. Due to the limitations of the JFP model to capture the behavior at high inertial numbers, the recently proposed Mandal and Khakhar (MK) model along with a normal stress difference law has been used to predict the flow properties for dense as well as dilute granular flows. In Appendix A, we first benchmark our numerical solution technique with analytical predictions of Parez *et al.* [51]. Since the analytical expressions derived by the authors assume a linear μ-I relation, we compare their theory only for $I \leqslant 0.35$. Next, we compare the DEM results with the predictions obtained using our numerical solution technique by employing two different rheological models.

A. Predictions from the JFP model

Figures 3(a)–3(f) show the variation of the velocity v_x, shear rate $\dot{\gamma}$, solids fraction ϕ, inertial number I, shear stress τ_{yx}, and viscosity $\eta = \tau_{yx}/\dot{\gamma}$ with distance y from the base at different times for $\theta = 24°$ and restitution coefficient $e_n = 0.5$. Black circles, red squares, and blue inverse triangles

Algorithm 1. Prediction of time-dependent flow properties.

---

1 Initialize $h = h_{min}$, $\phi(y) = \phi_{avg} = \phi_{max}$, $\epsilon = 10^{-5}$, temporal grid size $\Delta t = 0.1$, number of spatial grid points in y direction $N = 50$.
2 Obtain discrete positions $y = [0 : \Delta y : h]$ along the y direction using a uniform spatial grid spacing $\Delta y = h/N$.
3 Use Eq. (17a) for initial condition $v_x(y) = 0$ at $t = 0$.
4 while $t < t_{final}$ **do**
5   Calculate the following properties at time t.
6   Velocity gradient $|\dot{\gamma}| = dv_x(y)/dy$.
7   Inertial number $I(y)$ using Eqs. (14a) and (14b).
8   Solids fraction $\phi(y)$ using Eq. (9).
9   Pressure $P(y)$ using Eq. (11).
10   Shear stress $\tau_{yx}(y)$ using Eq. (15).
11   Solve Equation (16) with IC, BC1, and BC2 [Eqs. (17a)–(17c)] using PDEPE to obtain velocity $v_{x,next}$ at $t + \Delta t$.
12   Calculate the following properties at time $t + \Delta t$.
13   Velocity gradient $dv_{x,next}(y)/dy$.
14   Inertial number $I_{next}(y)$ using Eqs. (14a) and (14b).
15   Solids fraction $\phi_{next}(y)$ using Eq. (9).
16   Average solids fraction $\phi_{avg,next}$ by averaging the $\phi_{next}(y)$ across the bulk layer.
17   **if** $((||v_{x,next} - v_x||) > \epsilon$ **then**
18   Update the flowing layer thickness $h_{next} = h\phi_{avg}/\phi_{avg,next}$.
19   Recalculate discrete positions $y_{next} = [0 : \Delta y_{next} : h_{next}]$ along the y direction using a uniform spatial grid spacing $\Delta y_{next} = h_{next}/N$.
20   Assign $v_x(y) = v_{x,next}(y_{next})$, $\phi(y) = \phi_{next}(y_{next})$, $h = h_{next}$, and $\Delta y = h_{next}/50$.
21   Update time as $t = t + \Delta t$
22   **else**
23   Exit
24   **end**
25 end

---

represent the average DEM flow properties at $t = 100$, $t = 200$, and $t = 500$ time units. The solid lines represent the predictions at different times obtained by numerically solving Eq. (16) using the PDEPE solver and using the JFP model [Eq. (7)] for rheological description. The JFP model parameters obtained by fitting Eq. (7) to the simulation data are shown in Table I.

Figure 3(a) shows the variation of velocity v_x with distance y from the base at three different time instants of $t = 100$, $t = 200$, and $t = 500$ time units. The velocity profile shows a Bagnold dependence with negligible slip at the base and increases to a maximum value at the free surface. The velocity at the free surface keeps increasing with time, and the slope of the velocity profile near the base also changes. The shear rate near the base is a maximum and decreases with an increase in height from the base as can be seen in Fig. 3(b). The shear rate also increases with time at any given distance from the base. Figure 3(c) shows the inertial number I along the height of the flowing layer at different time instants. As expected, the inertial number also increases with time and shows minor variations in the layer for early times. At later times, it becomes nearly constant in most of the bulk layer with small oscillations.

Figure 3(d) shows the variation of solids fraction ϕ along the flowing layer at different time instants. The solids fraction ϕ shows large fluctuation across the flowing layer due to averaging over only a few snapshots. In addition, the usage of nearly monodisperse particles in the two-dimensional (2D) simulation may also lead to particle layering that can cause strong variations in solids fraction ϕ in different bins. With increasing time, a small decrease in solids fraction from $\phi \simeq 0.8$ to $\phi \simeq 0.75$ is observed. Figure 3(e) shows a linear variation of the shear stress τ_{yx} with distance y from the base due to the nearly constant bulk density of the layer. Figure 3(f) shows the viscosity $\eta = \tau_{yx}/\dot{\gamma}$ with distance y from the base. The viscosity varies nonlinearly from zero at the free surface to a maximum value at the base. With the increase in time, the viscosity decreases. The theoretical predictions obtained using the JFP rheological model are indeed able to capture the flow properties at different times for $\theta = 24°$.

Figures 4(a)–4(d) show the variation of the average velocity of the flowing layer, v_{avg}, average inertial number in the bulk, I_{bulk}, average solids fraction in the bulk, ϕ_{bulk}, and the slip velocity
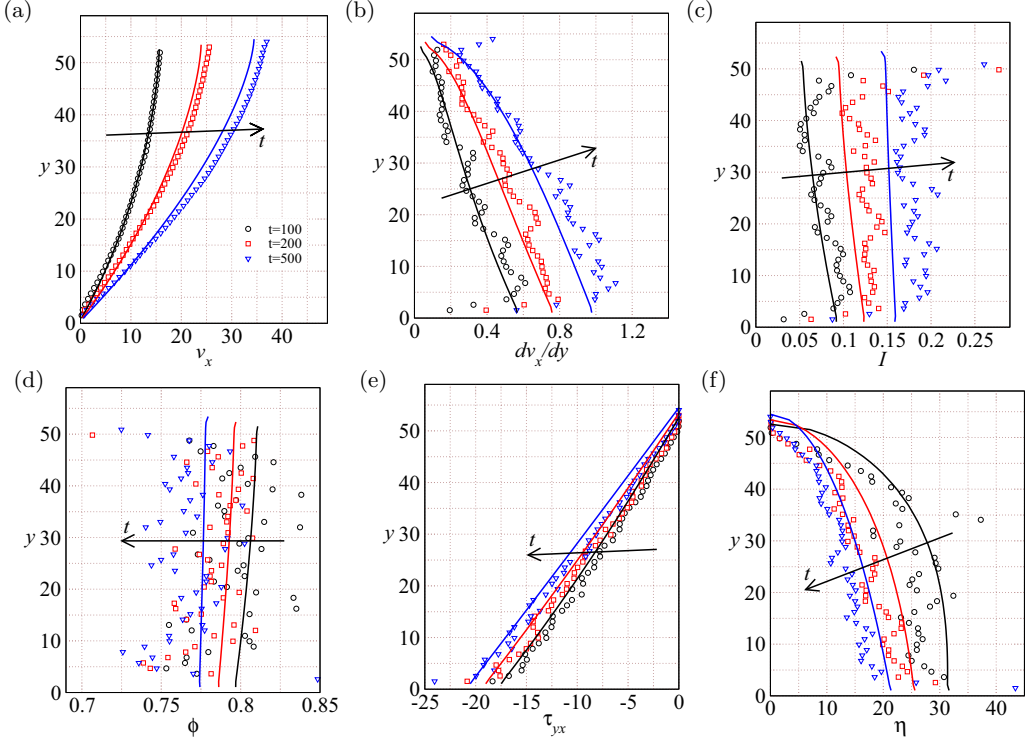
FIG. 3. Variation of the (a) velocity v_x, (b) shear rate $\dot{\gamma}$, (c) inertial number I, (d) solids fraction ϕ, (e) shear stress τ_{yx}, and (f) viscosity η with distance y from the base at different times for $\theta = 24°$. Symbols represent the DEM simulation data and the solid lines represent the JFP model predictions.

at the base, v_{slip}, with time t for inclinations varying from low to moderate inclination angles. The average velocity of the flowing layer, v_{avg}, is calculated as $v_{\text{avg}} = \frac{1}{h} \int_0^h v_x dy$. As expected, the average velocity increases with time and eventually becomes constant at a steady state. The steady-state value of the average velocity increases with an increase in inclination. Figures 4(b) and 4(c) show the variation of average inertial number and solids fraction in the bulk with time for different inclinations θ. The average values in the bulk are calculated by considering data in the bulk region ($0.2h \leqslant y \leqslant 0.8h$) of the layer and discarding the data near the free surface and the base where h is the free surface height. The inertial number also increases with time and eventually reaches a steady-state value and increases with the inclination angle. The bulk solids fraction decreases with time and inclination angle and eventually attains a steady state at large times.

Figure 4(d) shows the variation of slip velocity v_{slip} with time t for low to moderate inclinations. The slip velocity increases with an increase in inclination over time and eventually attains a steady

TABLE I. Model parameters for JFP model.

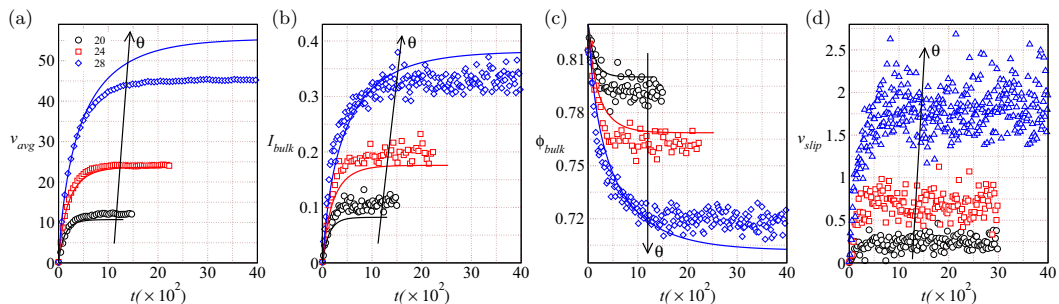| Expression	$e_n = 0.5$
$\mu(I) = \mu'_s + \frac{\mu'_m - \mu'_s}{1 + I'_0/I}$	$\mu'_s = 0.23$
	$\mu'_m = 0.69$
	$I'_0 = 0.20$

FIG. 4. Variation of the (a) average velocity of the layer, v_{avg}, (b) average inertial number in the bulk, I_{bulk}, (c) average solids fraction in the bulk, ϕ_{bulk}, and (d) slip velocity at the base, v_{slip}, with time t ($e_n = 0.5$) for different inclinations θ. Symbols represent the DEM simulation data whereas the solid lines in (a)–(c) represent the JFP model predictions.

state with small fluctuations around the steady mean slip velocity. The slip velocity in the case of these inclination angles is very small and neglecting the slip velocity in the calculation of average velocity barely affects the results. The effect, however, becomes important at higher inclinations and hence almost all the results reporting instantaneous and/or average velocity account for the slip velocity at the base in this study. Only the results shown in Fig. 21(b) in Appendix A assume the slip velocity at the base to be zero to remain consistent with the theoretical predictions of Parez *et al.* [51].

The solid lines in Fig. 4 represent the theoretical predictions obtained from the PDEPE solver using the JFP model. Figures 4(a)–4(c) show that the JFP model predicts the flow behavior very well for $\theta \leqslant 24°$. However, the JFP model predictions appear to be deviating from the DEM data for $\theta = 28°$. This can be attributed to the presence of normal stress difference which remains negligible for low inclinations but starts to become important as the angle increases [24,32]. Next, we consider even higher inclination angles and compare the predictions of the continuum model using the JFP model with DEM simulation results.

Figures 5(a)–5(d) show the variation of average velocity v_{avg}, average inertial number I_{bulk}, and average solids fraction ϕ_{bulk} for inclinations varying from $\theta = 30°$ to $\theta = 36°$. As before, the DEM simulations show that the average velocity and average inertial number increase with time and inclination angle and eventually attain a constant value after a sufficiently long time, indicating the existence of a steady state at all four inclination angles.
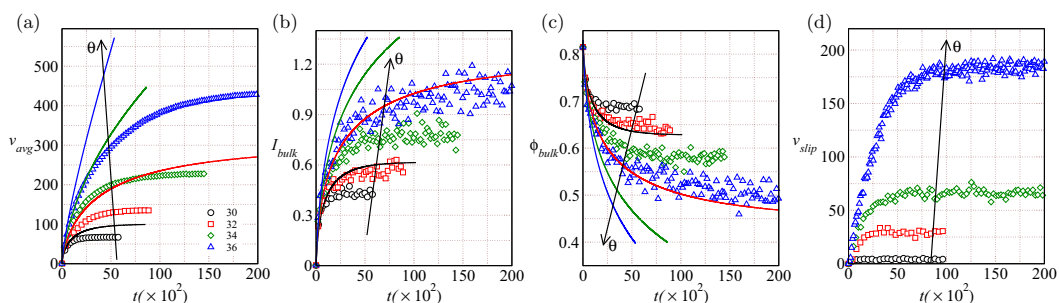

FIG. 5. Variation of the (a) average velocity of the layer, v_{avg}, (b) average inertial number in the bulk, I_{bulk}, (c) average solids fraction in the bulk, ϕ_{bulk}, and (d) slip velocity at the base, v_{slip}, with time t ($e_n = 0.5$) for different inclinations. Symbols represent the DEM simulation data whereas the solid lines in (a)–(c) represent the JFP model predictions.
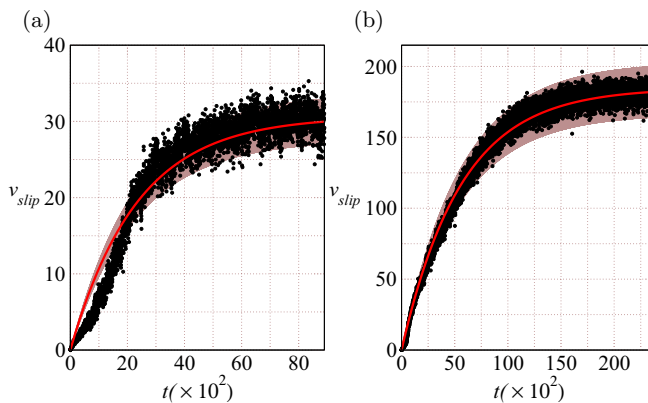
FIG. 6. Variation of the slip velocity v_{slip} with time t for $e_n = 0.5$ corresponding to (a) $\theta = 32°$ and (b) $\theta = 36°$. Black symbols represent the DEM simulation data. The solid red line represents the exponential fit to the DEM data. The brown band represents the modeled variation of the slip velocity used in the theoretical predictions by accounting for the fluctuations in the mean slip velocity.

The predictions using the JFP model (solid lines) capture the flow properties for moderate angles very well but fail to capture the flow behavior for high inclinations. Specifically, the theoretical predictions using the JFP model show continuously increasing average velocity and average inertial number for all $\theta \geqslant 32°$ and do not achieve a steady state during the time period of interest. The difference between the predicted values and DEM results keeps increasing with the inclination angle and the theoretical predictions for the higher angles (shown in Fig. 5) differ from the DEM results by a factor of 2. Similar differences are observed in the predictions of the average inertial number I_{bulk} and average solids fraction ϕ_{bulk} using the JFP model at higher inclinations. The predicted values of the average inertial number are found to be much higher and the average solids fractions are found to be substantially smaller than those observed in DEM simulations. Figure 5(d) shows that the slip velocity in the case of such high inclination angles is very significant. Neglecting such large slip velocity in the theoretical predictions affects the predicted values of the average velocity significantly.

Figure 6 shows the variation of the slip velocity v_{slip} with time t for two different angles $\theta = 32°$ and $\theta = 36°$. Although a small deviation from the fitted curve is evident at early times, the variation of the slip velocity with time is captured reasonably well using an exponential fit, shown using solid red lines in Fig. 6. A large scatter in the instantaneous slip velocity values is evident around the mean exponential variation. This scatter appears to be within 5–10 % of the mean value obtained from the exponential fit. In the results shown in this study (except Fig. 21 in Appendix A), the theoretical predictions utilize the fitted exponential time variation of the slip velocity while calculating the average velocity and instantaneous velocity profiles. The results for the shear rate, inertial number, packing fraction, shear stress, pressure, and apparent viscosity are not affected due to the presence of the slip velocity.

The results shown in this section confirm that the substantial difference observed between the DEM simulations and the theoretical predictions arise due to the inability of the JFP model to capture the rheology appropriately at high inclinations. In the next section, we show that the modified rheological description is able to capture the time-dependent properties in very good agreement with the DEM simulation results.

B. Predictions using modified rheological description

In this section, we report the predictions of the continuum model utilizing the new rheological description proposed by Patro et al. [32] which complements the MK model along with a normal
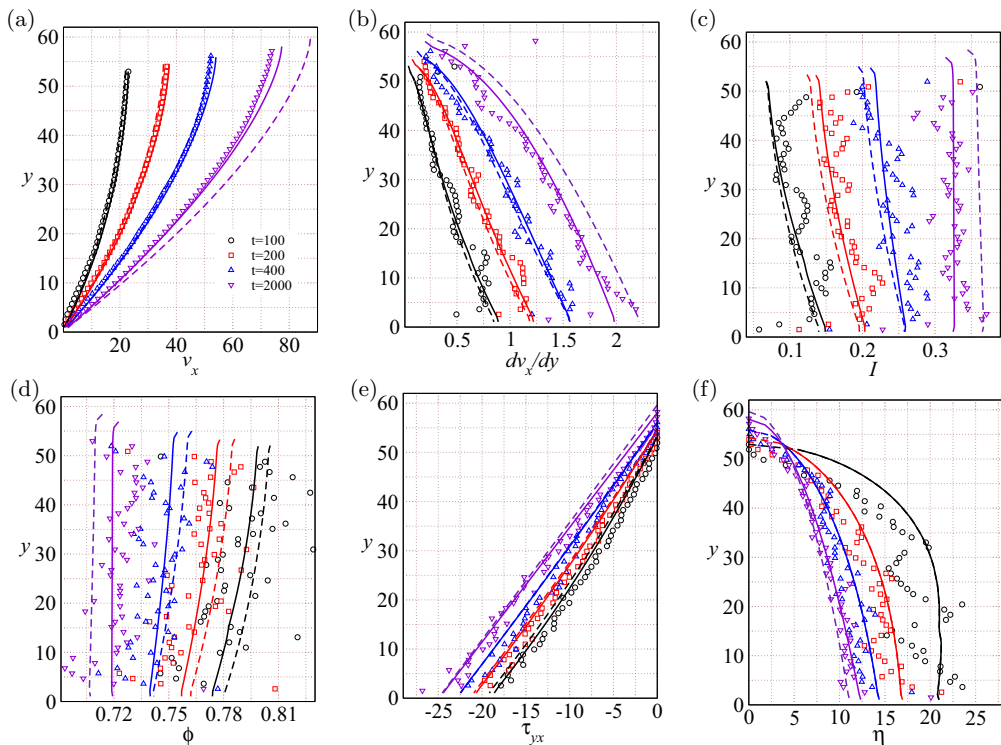
FIG. 7. Variation of the (a) velocity v_x, (b) shear rate $\dot{\gamma}$, (c) inertial number I, (d) solids fraction ϕ, (e) shear stress τ_{yx}, and (f) viscosity η with distance y from the base at different times for $\theta = 28°$. Symbols represent the DEM simulation data ($e_n = 0.5$), solid lines are the predictions of the modified rheology, and dashed lines represent the JFP model predictions.

stress difference law. Figures 7(a)–7(f) report the results for $\theta = 28°$ at four different time instances. Symbols represent the variation of velocity v_x, shear rate dv_x/dy, inertial number I, solids fraction ϕ, shear stress τ_{yx}, and viscosity $\eta = \tau_{yx}/\dot{\gamma}$ with distance y from the base. Black circles represent the flow properties at $t = 100$. Red squares represent the flow properties at $t = 200$. Similarly, blue triangles and purple inverse triangles represent the flow properties at $t = 400$ and $t = 2000$, respectively. The solid lines represent the theoretical predictions obtained from the continuum model using the modified rheology of Patro *et al.* [32]. The rheological model parameters for the modified μ-I relation, dilatancy law, and normal stress difference law are shown in Tables II, III, and IV, respectively. The predictions using the modified rheology are able to capture the flow properties very well at different times for $\theta = 28°$. For comparison, we also show the predictions obtained using the JFP model using dashed lines. The predictions for the JFP model differ marginally from the modified rheology predictions and DEM data for early times ($t \leqslant 1000$). At larger times, however, the JFP model predictions differ substantially from the DEM data.

TABLE II. Parameters for the MK model.

e_n	μ_s	c_1	c_2	I_0
0.1	0.26	0.92	0.36	0.69
0.5	0.24	0.68	0.22	0.39

TABLE III. Model parameters for the dilatancy law.

e_n	$\phi_{\max}$	a	α
0.1	0.82	0.30	0.99
0.5	0.82	0.31	1.00

This deviation of JFP model predictions at larger times becomes more evident from Figs. 8(a)–8(c). These figures show the variation of average velocity v_{avg}, average inertial number I_{bulk}, and average solids fraction ϕ_{bulk} with time t for three different inclinations. In all the cases, the predictions from the modified rheology (shown as solid lines) agree with the DEM simulation data better compared to the JFP model predictions shown using the dashed lines. While predicting the average velocity in Fig. 8(a), we account for the slip velocity at the base as mentioned before. However, assuming the slip velocity to be zero leads to very small differences in the flow predictions at these angles.

Figures 9(a)–9(c) show the variation of velocity v_x, inertial number I, and solids fraction ϕ with the distance from the base y using the modified rheology for $e_n = 0.5$ at $\theta = 36°$. The flow profiles observed in DEM simulations are indeed captured very well using the modified rheology (shown using solid lines). The JFP model, on the other hand, has serious limitations in predicting the flow properties (shown using dashed lines) accurately at such high inclinations. Specifically, the JFP model predictions lead to significant overpredictions of the velocity and inertial number and underprediction of the solids fraction at large times. Figures 9(d)–9(f) show the variation of average velocity v_{avg}, average inertial number I_{bulk}, and average solids fraction ϕ_{bulk} with time t for stiff inclinations in the range $32° \leqslant \theta \leqslant 40°$. The solid lines represent the predictions of the modified rheology [32]. For the higher values of inclination angles, the average inertial number exceeds unity. However, the modified rheological model is able to predict the transient flow properties in reasonable agreement with the DEM simulations.

As mentioned before, accurate prediction of velocity at high inclination requires reliable knowledge of the slip velocity at the base. Figures 10(a) and 10(b) show the variation of the slip velocity v_{slip} with the shear rate at the base, $\dot{\gamma}_{\text{base}}$, and the average inertial number I_{bulk}, respectively, using a semilogarithmic scale. The inset in Fig. 10(a) shows the variation of the v_{slip} with the $\dot{\gamma}_{\text{base}}$ in linear scale. A linear variation of the slip velocity $v_{\text{slip}} = l_{\text{slip}}\dot{\gamma}_{\text{base}}$ with a slip length of $l_{\text{slip}} = 1.48d$ is observed for low values of the dimensionless shear rate (up to 1.5). Similarly, the inset of Fig. 10(b) shows that a linear relation of v_{slip} with I_{bulk} is observed up to inertial numbers $I_{\text{bulk}} \sim 0.3$. We also show the variation of the ratio of the slip velocity to the average layer velocity, $v_{\text{slip}}/v_{\text{avg}}$, with the average inertial number I_{bulk} in Fig. 10(c). The $v_{\text{slip}}/v_{\text{avg}}$ ratio also shows a linear variation with the average inertial number up to $I_{\text{bulk}} \sim 0.3$. It appears that the slip velocity can be accurately predicted using a linear relation either with the shear rate or with the inertial number up to $I_{\text{bulk}} \sim 0.3$. However, a complex dependence of the slip velocity at large inertial numbers is observed in all three cases shown in Fig. 10. While it may be possible to describe this complex dependency using different functional forms for different ranges of inertial numbers, we refrain from doing that since this relationship will be highly dependent on the bumpiness as well as the frictional and dissipation characteristics of the base. Hence we use the simulation data to obtain a functional form describing

TABLE IV. Model parameters for the normal stress difference law.

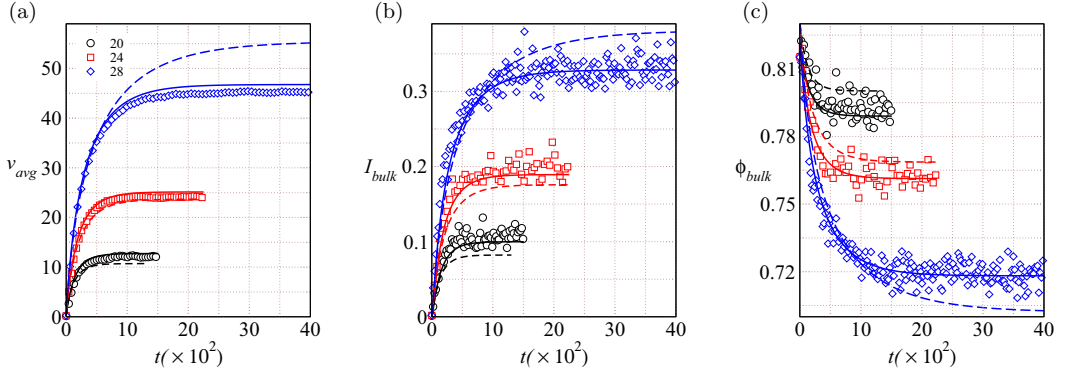| e_n	$I > I^* = 0.1$			$I \leqslant I^* = 0.1$
	A	B	C	K
0.1	0.16	0.39	-0.1	-0.06
0.5	0.10	0.43	-0.1	-0.06

FIG. 8. Variation of the (a) average velocity of the layer, v_{avg}, (b) average inertial number in the bulk, I_{bulk}, and (c) average solids fraction in the bulk, ϕ_{bulk}, with time t for different inclinations θ. Symbols represent the DEM simulation data ($e_n = 0.5$), solid lines are the predictions of the modified rheology, and dashed lines represent the JFP model predictions.
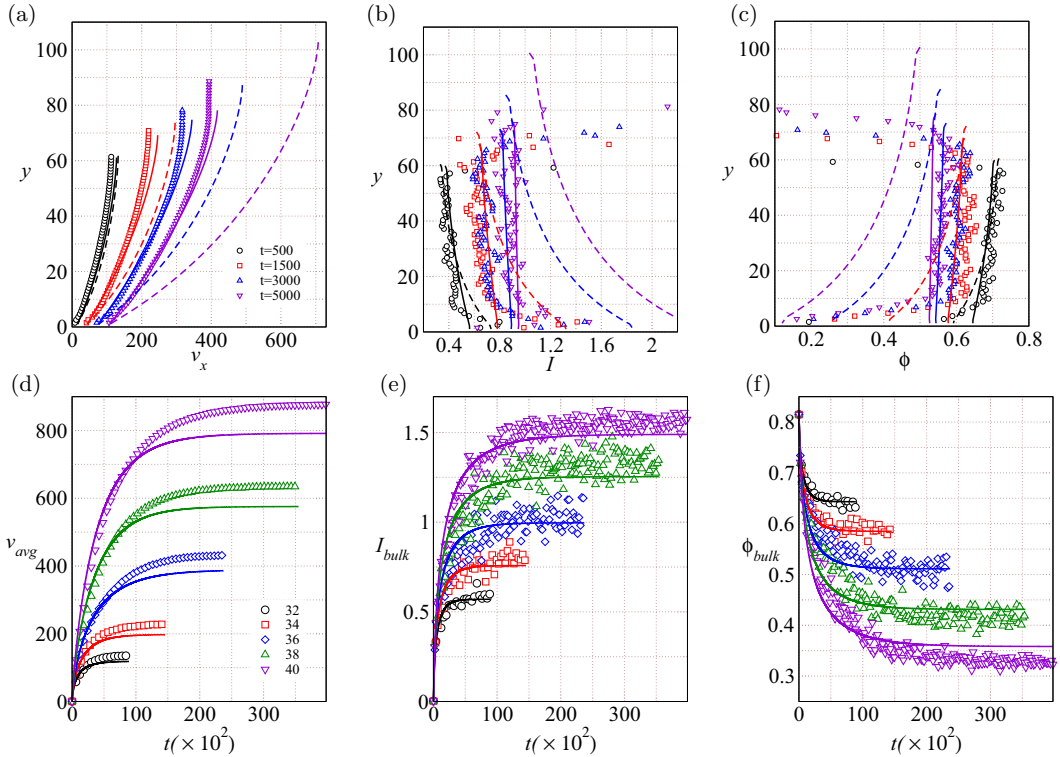

FIG. 9. Variation of the (a) velocity v_x, (b) inertial number I, and (c) solids fraction ϕ with distance y from the base at different times for $\theta = 36°$. Variation of the (d) average velocity of the layer, v_{avg}, (e) average inertial number in the bulk, I_{bulk}, and (f) average solids fraction in the bulk, ϕ_{bulk}, with time t for even inclinations $32° \leqslant \theta \leqslant 40°$. Symbols represent the DEM simulation data ($e_n = 0.5$), solid lines are the predictions of the modified rheology, and dashed lines represent the JFP model predictions.
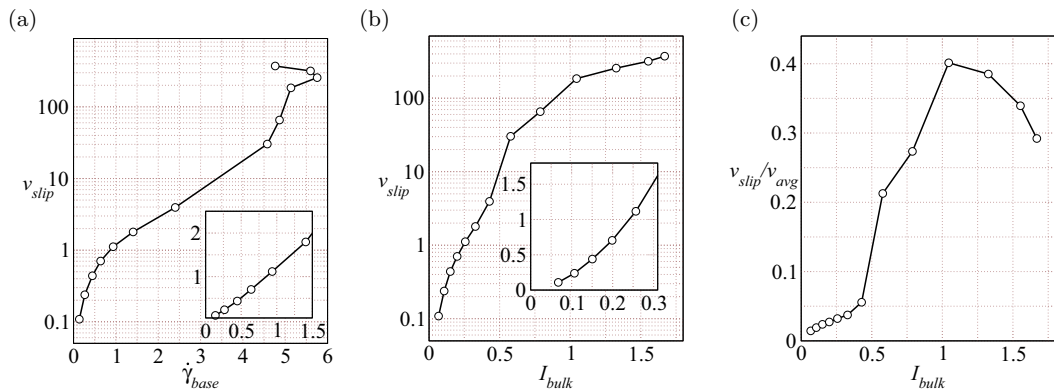
FIG. 10. Variation of the slip velocity v_{slip} with (a) the shear rate at the base, $\dot{\gamma}_{\text{base}}$, and (b) average inertial number I_{bulk} on a semilogarithmic scale. The insets show the main figure data on a linear scale over a smaller range. (c) Variation of the ratio of the slip velocity to the average velocity, $v_{\text{slip}}/v_{\text{avg}}$, with the average inertial number I_{bulk}. The data for all three cases correspond to steady-state flow corresponding to $e_n = 0.5$.

slip velocity v_{slip} as a function of time t data in our theoretical predictions. These slip velocities for the three higher angles $\theta = 34°$, $\theta = 38°$, and $\theta = 42°$ are reported in Figs. 11(d), 11(e), and 11(f), respectively. Despite small deviations from the mean trend, an exponential variation describes the slip velocity dependence on time very well. All the data seem to be within 5% of the fitted mean slip velocity. In the predictions of properties shown in Figs. 11(a)–11(c), the fitted mean slip velocity with time is accounted for. This accounting of the mean slip velocity is crucial for accurate predictions of the average and instantaneous velocities. Other properties, however, do not get altered by ignoring the slip velocity at the base. Figures 11(a)–11(c) report the results for highly dissipative particles with $e_n = 0.1$ spanning a large range of inclinations. Symbols represent the DEM data and the solid lines represent the modified rheological model predictions of Ref. [32]. Figures 11(a)–11(c) report the average flow properties for moderate to high inclinations (i.e., $\theta = 30°$, $34°$, $38°$, and $42°$). The results for inclinations $\theta \leqslant 30°$ are shown in the inset. The steady-state average velocity varies from $v_{\text{avg}}^{ss} \sim 10$ at $\theta = 20°$ to $v_{\text{avg}}^{ss} \sim 580$ at $\theta = 42°$. The average inertial number varies from around $I_{\text{bulk}} \sim 0.1$ at the lowest inclination to $I_{\text{bulk}} \sim 1.5$ for the highest inclination. The modified rheology is able to predict the entire range of velocity profiles, inertial number, and solids fraction observed across these different inclination angles accurately.

V. DISCUSSION

A. Importance of granular dilatancy

The modified μ-I rheological model along with a normal stress difference law is able to predict flow profiles at large inclination angles that are in good agreement with the DEM simulation results. However, this accurate prediction requires the continuum approach to keep track of the free surface. In this work, we have utilized a simplified method to account for the variation of the flowing layer thickness $h(t)$ with time t. Using the mass balance and equating the total mass at any instant to be equal to the mass at $t = 0$, the flowing layer thickness h at every instant is updated by $h(t) = h_{\min}\phi_{\max}/\phi_{\text{avg}}(t)$. Most of the studies dealing with granular rheology assume the flow to be incompressible and hence do not bother about such dilation effects. In order to check if this increase of the layer height with time is critical to get accurate flow properties, we also perform continuum simulations assuming that the flowing layer thickness remains constant for the entire range of inclination angles. Note that the continuum predictions for the velocity obtained by solving Eq. (16) do not predict any slip velocity (which is added to the predictions for comparison with DEM data). Hence we compare the predictions for $v_{\text{avg}} - v_{\text{slip}}$ with time t in Fig. 12.
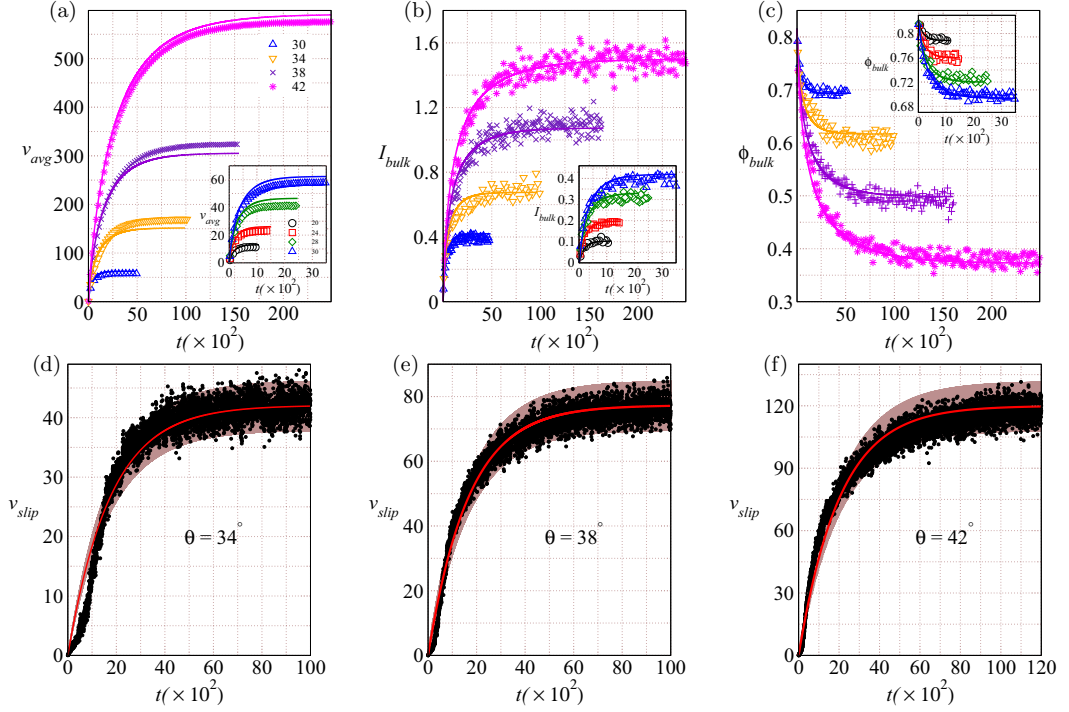
FIG. 11. Variation of (a) the average velocity of the layer, v_{avg}, (b) the average inertial number in the bulk, I_{bulk}, and (c) the average solids fraction in the bulk, ϕ_{bulk}, with time t at different inclinations θ. Symbols represent the DEM data for $e_n = 0.1$ whereas the solid lines represent the theoretical predictions obtained from the modified rheology. Inset shows the results for low to moderate inclinations. The results for higher inclination angles are reported in the main figure. Slip velocity at the base, v_{slip}, as a function of time for inclination (d) $\theta = 34°$, (e) $\theta = 38°$, and (f) $\theta = 42°$. The red line shows the exponential fit to the simulation data (shown using black circles). The brown band shows the variation of 5% from the mean velocity and is able to capture the slip velocity data at all times.
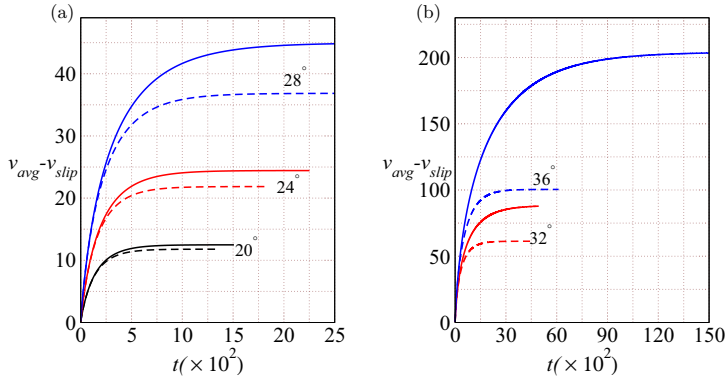

FIG. 12. Variation of the average velocity of the layer, v_{avg}, with time t for $e_n = 0.5$ at (a) $\theta = 20°$, 24°, and 28° and (b) $\theta = 32°$ and 36°. The lines are the theoretical predictions from the modified rheological model. Solid lines are predictions considering variable flowing layer thickness, while dashed lines are predictions considering a constant flowing layer thickness.
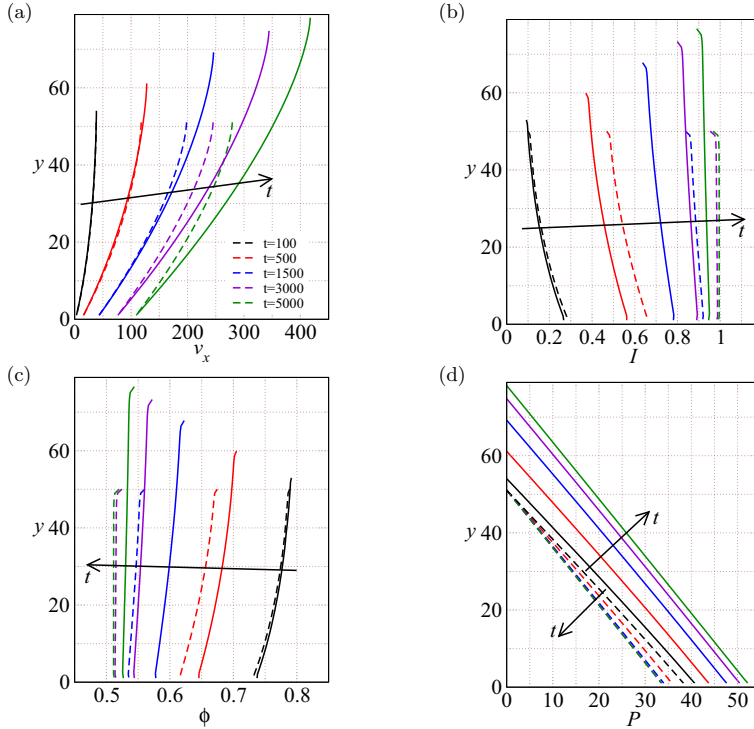
FIG. 13. Variation of the (a) velocity v_x, (b) inertial number I, (c) solids fraction, and (d) pressure P with distance y from the base at different times for $e_n = 0.5$ at $\theta = 36°$. The solid lines are the theoretical predictions from the rheological model considering variable flowing layer thickness. The dashed lines are the theoretical predictions from the rheological model considering constant flowing layer thickness.

Figure 12(a) shows the variation of $v_{avg} - v_{slip}$ for $\theta = 20°$, 24°, and 28°. The average velocity predicted by assuming a constant flowing layer thickness is close to the predictions for variable flowing layer thickness at low inclinations. As the angle of inclination increases, the deviation between the constant flowing layer thickness case and the variable flowing layer thickness case starts to increase, as evident in Fig. 12(b). These results confirm that the effect of the layer dilation becomes crucial and needs to be accounted for at high inclinations. This can be seen more clearly in Figs. 13(a)–13(d), where the constant layer thickness predictions start deviating from the variable layer thickness predictions at $t = 500$ and become much larger at higher times. Note that the velocity [shown in Fig. 13(a)] across the layer for the two cases at $t = 500$ differs only near the free surface. However, the inertial number and the solids fraction at $t = 500$ for the two cases differ significantly all across the layer. This noticeable difference between the two cases can be understood in the following manner. With the increase in the velocity, the shear rate and, hence, the inertial number I increase with time. This increase in I causes the solids fraction ϕ (and hence bulk density $\rho_b = \phi \rho_p$) to decrease. In the constant-height case, the reduction in the bulk density leads to a small reduction in the pressure [dashed lines in Fig. 13(d)] with time. Since $I = \dot{\gamma} d/(\sqrt{P/\rho_p})$, this small reduction in pressure contributes to the increase of the inertial number only marginally, and most of the contribution to the inertial number increase is due to the change in the shear rate. However, when the dilation of the layer is allowed, the height of the layer increases and hence the pressure at all locations in the layer increases with time [solid lines in Fig. 13(d)]. This increased pressure leads to a reduction in the inertial number while the shear rate increase leads to an increase in the inertial number. Figure 13(b) shows that the net effect of these two competing influences of shear rate and
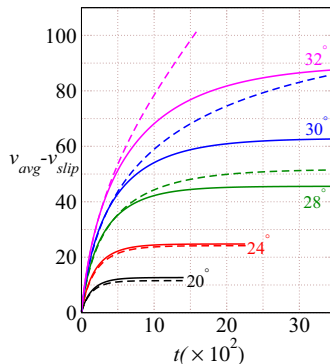
FIG. 14. Variation of the average velocity of the layer, v_{avg}, with time t for $e_n = 0.5$ at $\theta = 20°$, $24°$, $28°$, $30°$, and $32°$. Solid lines are predictions considering normal stress difference, while dashed lines are predictions without considering the effect of normal stress difference.

pressure effectively leads to an increase of I. However, this increment in I is smaller compared to the constant-height case due to the increase in pressure. With time, the inertial number increases and the change in pressure becomes even more prominent and the discrepancy between the variable- and constant-layer-height cases keeps increasing.

B. Role of normal stress difference

One of the key features of the rheology proposed by Patro *et al.* [32] is the significant role of the normal stress difference due to the anisotropy in the diagonal components of the stress tensor. This stress anisotropy, along with the nonmonotonic μ-I relation, makes the rheological description complete. The JFP model, on the other hand, ignores the stress anisotropy and assumes the normal stress difference to be zero. In order to explore the importance of normal stress differences in predicting the flow properties accurately, we predicted the average velocity by ignoring the normal stress differences and using only the nonmonotonic μ-I variation. As shown in Fig. 12, the slip velocity has not been included in these predictions. These predictions are found to be nearly identical to the predictions accounting for the presence of the normal stress difference for $\theta \leqslant 24°$. This is due to the fact that the ratio of normal stress difference to pressure is very small at low inclinations (i.e., at low inertial numbers). However, at higher inclinations, the difference between the solid and dashed curves of the same color becomes significant (Fig. 14), confirming that the presence of normal stress difference cannot be ignored at higher inclinations, i.e., at $\theta = 30°$ and $\theta = 32°$. These results indicate that accounting for the nonmonotonic variation of μ-I alone is not enough to capture the flow properties accurately for flows at high inertial numbers (observed at high inclinations).

C. Oscillatory flow at high inclinations

Figure 15 shows the snapshots of the flowing layer ($e_n = 0.5$) for an inclination of $\theta = 42°$ at four different time instants. Starting from a packed arrangement of particles at $t = 0$, the layer height increases as the flow evolves with time and achieves more than twice the initial layer height. The reduction in the solids fraction accompanied with this layer height increase is evident from the sparse arrangement of particles in the bed. Few studies identify a clustering instability phenomenon that occurs when the uniform shear flow breaks into alternate bands of dense and dilute clusters of particles and reported that this phenomenon is caused by the coupling between the density and the velocity fluctuations [76,78]. Note that the region near the base depicts a lower solids fraction compared to the bulk of the layer. In addition, the arrangement of particles in the layer shows regions
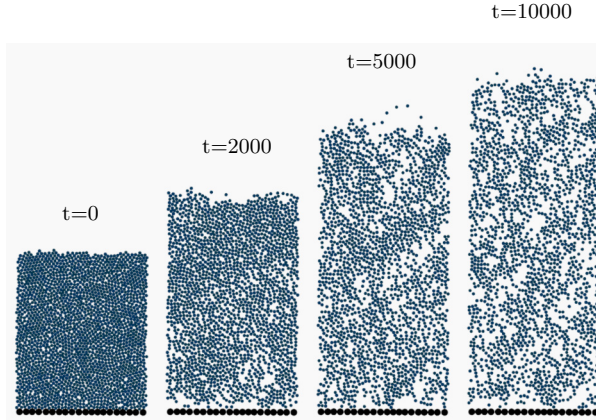
FIG. 15. Snapshots of the system configuration at different times for $e_n = 0.5$ at $\theta = 42°$.

of varying density along the flow as well as in the normal direction. These density variations at high angles are observed along with noticeable fluctuations in the layer height.

These oscillations in the bulk layer height h_{bulk} are shown in Fig. 16(a) over a time period of 200 time units starting from a time instant t_0. Oscillations in the center of mass, y_{com}, are shown in Fig. 16(b). These height measurements are done after the flow has achieved steady kinetic energy (hence t_0 varies with the inclination angle θ). The oscillations in the bulk layer height h_{bulk} as well as center of mass, y_{com}, keep increasing with the inclination angle. While the difference between maximum and minimum bulk height is around a couple of particle diameters for inclinations $\theta \leqslant 30°$, this variation becomes as large as $\Delta h_{\text{bulk}} \approx 16d$ for the $\theta = 42°$ case [Fig. 16(a)]. As shown in Fig. 16(b), the amplitude of the oscillations observed in the center-of-mass position is approximately half of that observed in the bulk layer height. These large-amplitude oscillations in the layer height at high inclinations might be linked to the pressure (or expansion) waves that cause density variations in the system. Such variations are observable in the video link given in Ref. [77] (see Appendix C). These effects indicate that the role of density and height variations become important and cannot be ignored for granular flows at inertial numbers comparable to unity. Such oscillations at high chute inclinations have been mentioned by Brodu *et al.* [26] as well. Due to these oscillations, the calculation of rheological parameters in Ref. [32] from simulation data at high inclinations requires averaging over a large number of snapshots so that the influence of these fluctuations is averaged
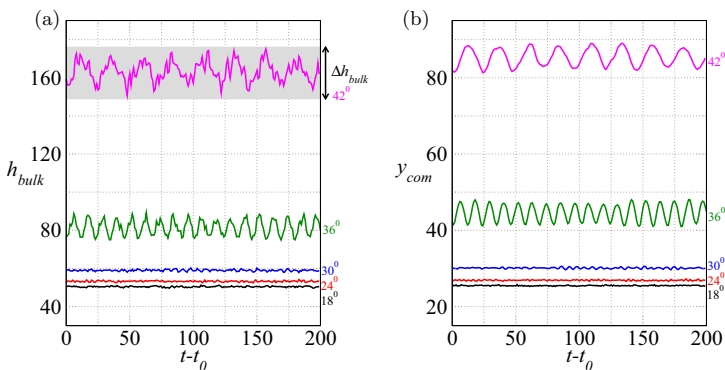

FIG. 16. Steady-state oscillating behavior of (a) bulk flowing layer thickness h_{bulk} and (b) center of mass y_{com} at different inclinations for restitution coefficient $e_n = 0.5$.
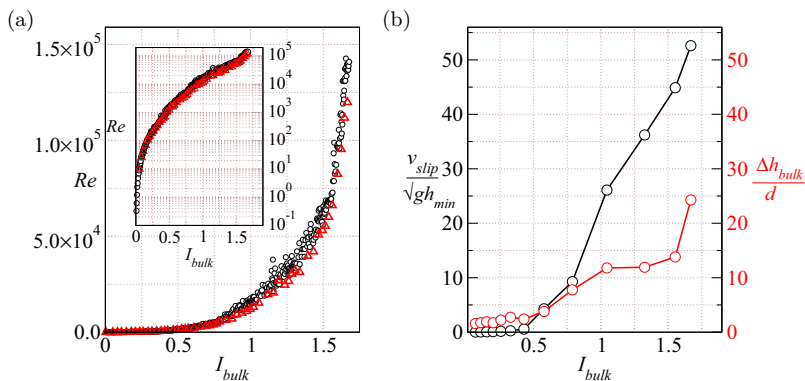
FIG. 17. (a) Variation of the Reynolds number Re with the average inertial number in the bulk, I_{bulk}, for restitution coefficient $e_n = 0.5$. The inset in (a) shows the variation of the Reynolds number (Re) with the average inertial number (I_{bulk}) in the semilogarithmic scale. Black circles correspond to h_{max} whereas the red triangles correspond to h_{bulk} for the layer thickness in Reynolds number calculation. (b) Variation of the slip velocity $v_{\text{slip}}/\sqrt{gh_{\text{min}}}$ and $\Delta h_{\text{bulk}}/d$ (on the right ordinate) with the average inertial number I_{bulk} at steady state.

out. Furthermore, the data near the free surface and chute base are ignored during the rheological parameter estimation as Mandal and Khakhar [27] have shown that the μ-I data near the free surface and base follow slightly different behavior as compared to the data in the bulk region.

In classical fluids, as the flow becomes faster, the competition between the inertia and gravity leads to instability and the free surface shows long wave modulations. In the case of turbulent flows, this instability is known as roll wave instability, while in the case of viscous fluids, it is referred to as Kapitza instability. Such instabilities have been experimentally observed in the case of granular media before [79]. Since our simulations use a periodic box, such long wave undulations are not observable. However, the oscillations in layer height [as shown in Fig. 16(a)] might be indicative of such instability in the flow. A pronounced rippling behavior in the case of gravity-driven free surface flow of Newtonian fluids occurs in the range of Reynolds numbers $20 \leqslant \text{Re} \leqslant 1500$ [80]. Beyond this Reynolds number, the flow of Newtonian fluids becomes chaotic and is considered to be turbulent.

Since the granular flow behavior is controlled by inertial number, we plot the variation of the Reynolds number Re of the layer with the average inertial number I_{bulk} in Fig. 17(a). Calculation of the Reynolds number for a fluid requires knowledge of its density and viscosity. While the bulk density of the flowing granular fluid remains constant across most of the layer, the viscosity $\eta = \tau_{yx}/\dot{\gamma}$ keeps changing across the layer [see Fig. 7(f)]. In the absence of a proper definition of Reynolds number for granular flows, we use the average density ρ_{avg} and average viscosity η_{avg} of the layer by averaging these properties in the bulk region, i.e., the region away from the base and the free surface. The average velocity v_{avg} is calculated by averaging across the entire flowing layer. Using these average values, the Reynolds number for the layer is calculated as $\text{Re} = \frac{\rho_{\text{avg}} v_{\text{avg}} h}{\eta_{\text{avg}}}$. The calculation of Reynolds number using $h = h_{\text{max}}$ is shown using black circles whereas the calculation based on $h = h_{\text{bulk}}$ is shown using red triangles in Fig. 17(a). The difference between the two seems to become significant only at large inertial numbers.

Figure 17(b) shows the variation of scaled slip velocity $v_{\text{slip}}/(gh_{\text{min}})^{0.5}$ with the average inertial number I_{bulk}, where h_{min} is the minimum layer thickness in the packed configuration at the beginning of the simulation. The scaled slip velocity becomes significantly different from zero for inertial numbers $I_{\text{bulk}} > 0.5$. The difference in the maximum and minimum value of the bulk flowing layer thickness ($\Delta h_{\text{bulk}}/d$, shown on the right ordinate) remains nearly constant for $I_{\text{bulk}} < 0.5$ and shows a noticeable increase for higher inertial numbers. A close look at the inset of Fig. 17(a), which shows the main graph on a semilogarithmic scale, indicates that $I_{\text{bulk}} \approx 0.5$ corresponds to $\text{Re} \approx 1500$. As
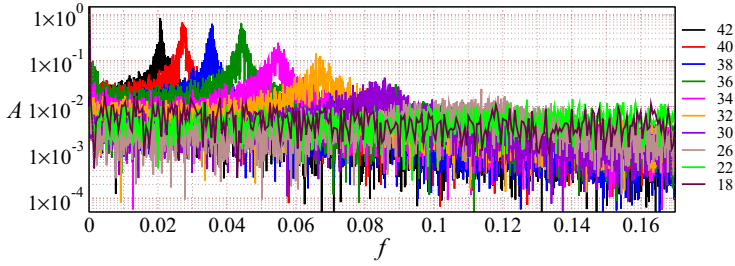
FIG. 18. Fast Fourier transform analysis of the center-of-mass data for all inclination angles.

mentioned before, this limit of Reynolds number corresponds to the onset of turbulence in the case of Newtonian fluids. Whether the noticeable changes in the slip velocity and the bulk layer height oscillations observed in the flow correspond to onset of turbulence in the flowing granular layer is an open question that remains to be explored. For the sake of completeness, it is worth mentioning that the limit Re = 20 for the onset of rippling flow corresponds to $I_{\text{bulk}} \approx 0.07$.

In order to investigate the time-periodic behavior of the layer at high inertial numbers, we performed a fast Fourier transform (FFT) analysis of the time series data of the center-of-mass position at steady state. Figure 18 shows the amplitude spectrum of the center of mass for different inclinations. The amplitude spectrum for inclinations $\theta = 18°$ and $\theta = 22°$ shows nearly uniform distribution for all frequencies. At higher inclinations, a dominant frequency with a clear peak starts to appear. The occurrence of a dominant frequency in the amplitude spectrum confirms that the variation of layer height occurs with a characteristic time period at these large inclinations. The peak frequency keeps moving to lower values as the inclination angle increases, indicating that the time period of oscillations increases with the inclination angle. Figure 18 also shows that the amplitude of oscillations at $\theta = 42°$ is nearly two orders of magnitude higher compared to those at $\theta = 26°$. Hence the oscillations observed in the layer at high inclinations are of larger amplitude and occur over larger time periods compared to those at moderate inclinations.

FFT analysis of the bulk layer height and the kinetic energy data are shown for three different inclinations in Fig. 19 using red and blue lines, respectively. The black lines in the figure correspond
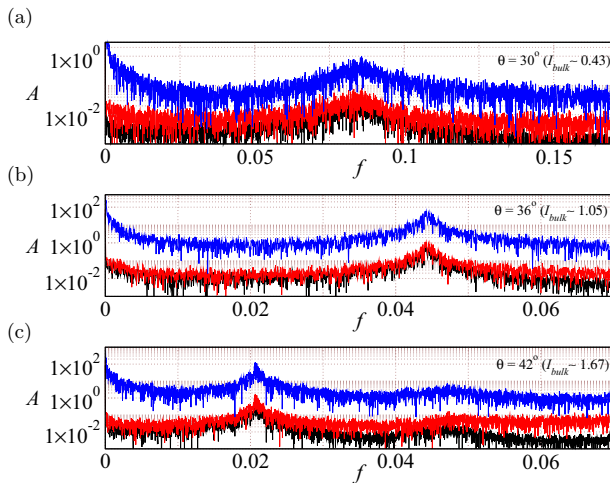

FIG. 19. Fast Fourier transform analysis of the center of mass (black line), bulk flowing layer thickness (red line), and kinetic energy (blue line) for inclination angle (a) $\theta = 30°$, (b) $\theta = 36°$, and (c) $\theta = 42°$.
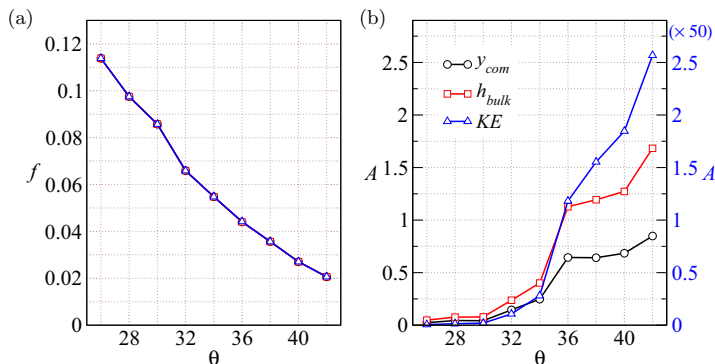
FIG. 20. (a) Variation of the dominant frequency f corresponding to different inclination angles θ. (b) Variation of the amplitude A corresponding to the dominant frequency f [shown in (a)] for different inclination angles. See text for details.

to the center-of-mass position. The maximum amplitude of the spectrum is observed at the same frequency for all three properties. Hence we conclude that the oscillations at high inclinations affect these properties of the flow in a nearly identical fashion. This is more clearly observed in Fig. 20(a), which shows that the dominant frequency for all three properties is identical at any given inclination. The figure also shows that the oscillation frequency decreases with an increase in the inclination angle. Figure 20(b) shows that the amplitude of oscillations increases with the inclination angle and the amplitude of the oscillations in the bulk layer height is approximately twice of that in the center of mass. The kinetic energy oscillation amplitudes (shown by blue on the right ordinate) differ by nearly two orders of magnitude. Note that the data for angles less than $24°$ cannot be included due to the lack of any dominant frequency in the amplitude spectrum. Figure 20(a) shows that the dominant frequency for $\theta = 30°$ is found to be $f \approx 0.09$. The corresponding values for $\theta = 36°$ and $\theta = 42°$ are found to be $f \approx 0.04$ and $f \approx 0.02$, respectively. In order to get an estimate of the frequencies that might be observed in experiments, the dimensionless dominant frequencies reported above need to be converted to dimensional values. For 1-mm particles flowing under the influence of earth's gravity, these frequencies turn out to be approximately 9 Hz for $\theta = 30°$, 4 Hz for $\theta = 36°$, and 2 Hz for $\theta = 42°$. Such oscillations have been reported in recent experimental studies of chute flow of granular materials by Bachelet *et al.* [18] as well. Given the significant differences between the inclination angle, flowing layer thickness, and the presence of sidewalls, a quantitative comparison of our results with their observation is not appropriate.

VI. SUMMARY AND FUTURE WORK

We perform two-dimensional DEM simulations of granular materials flowing down a bumpy inclined plane varying over a wide range of inclination angles and calculate various flow properties of interest as the flow evolves with time and achieves a steady state. We also obtain numerical solutions of the momentum balance equations [Eq. (1)] supplemented by different constitutive rheological models [Eqs. (7) and (8)] using the PDEPE solver in MATLAB. This solver uses an implicit finite difference method to solve the resulting partial differential equation [Eq. (16)]. The numerical simulation assumes a fully developed flow so that it can be compared with the DEM simulations of flow over a chute having periodic boundary conditions. We first utilize the nonlinear μ-I relation of the JFP model [37] to predict various time-dependent flow properties. The predictions obtained from the numerical solutions are compared with the DEM simulations and are found to be in good agreement with the DEM simulations for inclination $\theta < 28°$. Differences in the predictions of average velocity v_{avg} become noticeable for $\theta = 28°$ ($I \sim 0.3$) and this difference is attributed to the neglect of normal stress difference in the JFP model. The JFP model fails to capture the flow

behavior for $\theta > 28°$ as it reaches higher inertial numbers. The deviation between predictions and DEM data keeps increasing with the inclination angle θ and no steady flow is predicted for $\theta \geqslant 36°$ using the JFP model, which is inconsistent with the DEM results.

Next, we predicted the flow properties using the modified μ-I rheology along with the normal stress difference law recently proposed by Patro *et al.* [32]. The method also accounts for the dilation of the layer with an increase in the inertial number as the flow evolves with time. The predicted flow properties obtained using the modified rheological model are in very good agreement with the DEM simulation results for a much larger range of inclinations (up to $\theta = 40°$). In the numerical predictions of the velocity profile, the slip velocity needs to be explicitly accounted for and cannot be neglected at large inclinations. To summarize, we find that accurate prediction of time-dependent flow properties at high inertial numbers requires us to account for the following effects: (1) the nonmonotonic μ-I relation proposed by Patro *et al.* [32], (2) the presence of the normal stress difference, (3) the presence of the slip velocity at the chute base, and (4) dilation of the flowing layer to account for changes in the solids fraction. Ignoring any of these effects leads to significant errors in the predictions at high inclinations.

Continuum simulations of granular flows using different rheological models have been actively pursued since the last few years. However, all such studies have remained limited to inertial numbers less than unity. This work shows that accounting for these four important effects is crucial for a successful and reliable continuum simulation of high-speed granular flows. It is worth highlighting that the numerical solution of the momentum balance equations does not capture the periodic oscillations in the flow properties at steady state which become prominent at high inclinations. The bulk layer height, the center-of-mass position of the layer, as well as the kinetic energy show oscillations around the steady-state value with a characteristic frequency beyond an inclination angle. As the inclination angle increases, both the amplitude and time period of the oscillations increase. Despite the periodic variations observed at high inclinations, the time-averaged properties are predicted reasonably well using the modified rheology proposed in Ref. [32].

It has been shown by Barker *et al.* [48] that the μ-I rheology given by the JFP model is ill posed at high and low inertial numbers. In other words, for a given set of rheological parameters, there exist a minimum and a maximum value of the inertial number beyond which the results obtained from solving the rheological and momentum balance equations will be grid size dependent. However, the variation of the effective friction coefficient with the inertial number assumed in such studies is not consistent with the simulation results. Hence a detailed study about the well-posedness of the rheological model of Patro *et al.* [32] by accounting for the presence of the normal stress difference and nonmonotonic variation of μ with I needs to be pursued. Furthermore, the compressibility effects also need to be accounted for. In order to check the grid size effect on our predictions, we obtained theoretical predictions using three different grid sizes for the modified rheology case and the results were found to differ from each other by less than 1%. Furthermore, the results obtained from the modified rheology are found to be in excellent agreement with the DEM simulations. Hence these results give us confidence that the proposed rheology is able to predict the time-dependent behavior of granular flows at high inertial numbers.

Most studies using continuum modeling for granular materials treat them as incompressible fluids. Such a treatment for granular flows in silos, hoppers, heaps, etc., may not lead to significant errors since such flows are typically restricted to $I \leqslant 0.5$. However, free surface flows in avalanches and long chutes at high inclinations may show flows at higher inertial numbers. Our results, although reported for two dimensions, show that ignoring the dilatancy effects in such cases for $I > 0.6$ may lead to inaccurate predictions. The presence of normal stress difference reported in the work suggests that the rheology of granular materials in three dimensions at high inertial numbers will require accounting for both the first and second normal stress differences. A detailed study investigating the study of three-dimensional (3D) granular chute flows at high inertial numbers for the transient as well as steady state will be reported in the future. While the solids fraction across the layer remains nearly constant in the case of chute flow, the presence of sidewalls leads to the variation of the inertial number and hence the solids fraction across the layer in the case of heap

flows. Since the modified rheological model of Patro *et al.* [32] seems to be applicable for both dilute as well as dense granular flow regimes, it can also be utilized to explore the liquid-gas transition that occurs in heap flows confined between two sidewalls at high flow rates [3,81]. The high-speed granular flows observed at large inertial numbers are accompanied with low solids fractions. The kinetic-theory-based modeling of these dilute, rapid flows have been developed over the last few decades and detailed theoretical formulations exist in this framework. In addition, a lot of work is also available on the role of slip velocity and boundary conditions in the framework of the kinetic theory. A separate work devoted to detailed comparison of the kinetic theory predictions with the DEM results is currently under investigation and will be communicated in near future.

The data that support the findings of this study are available from the corresponding author upon request.

APPENDIX A: ANALYTICAL AND NUMERICAL PREDICTIONS FOR LINEAR μ-I MODEL

In this section, we compare the predictions of average velocity v_{avg}, average inertial number in the bulk, I_{bulk}, and average solids fraction in the bulk, ϕ_{bulk}, using the analytical solution given by Parez *et al.* [51]. The authors predicted the flow properties for unsteady flows flowing down an inclined plane using an analytical approach. They considered a linear form of the μ-I model and their results were in very excellent agreement with their DEM simulation results. Due to the weak dependence of solids fraction on the flow velocity reported in previous works [2,19,20,34,82], the authors assumed a constant solids fraction in their analytical approach to derive the expression for time-dependent flow properties. The authors obtained a series solution for the shear rate and the velocity profile. The solution can be very well approximated by a single-term solution and ignoring other terms of the series since they are much smaller compared to the first term. This analytical solution for the time-dependent velocity profile was derived using a linear relation between the effective friction coefficient $\mu(I)$ with inertial number I, i.e., $\mu(I) = \tan\theta_r + bI$. The values of the model parameters $\tan\theta_r$ and b are obtained by fitting a line to the μ-I data obtained from DEM simulations as shown in Fig. 21(a). In order to ensure a linear μ-I relation, only data up to $\theta \leqslant 28°$ are considered in Fig. 21(a). The value of the slope and intercept of the fitted line are obtained to be $b = 0.76$ and $\tan\theta_r = 0.29$. The solid lines in Figs. 21(b)–21(d) show the flow properties such as the average velocity, the average inertial number, and the average solids fraction predicted using the single-term analytical solution. We use the following expressions reported by Parez *et al.* [51] for velocity:

$$v(y,t) = \frac{2}{3}\frac{\sqrt{\phi_s g \cos\theta}(\tan\theta - \tan\theta_r)}{bd}\left(h_s^{3/2} - y^{3/2}\right)(1 - e^{-t/T_1}) + \text{higher-order terms}, \quad \text{(A1)}$$

where $T_1 = 0.5\sqrt{\phi_s}\frac{h_s^{3/2}}{bd\sqrt{g\cos\theta}}$. The average inertial number I_{bulk} is calculated using Eq. (13) where the shear rate is obtained by numerically differentiating the velocity predicted from the theory of Parez *et al.* [51] and the pressure is assumed to be equal to hydrostatic pressure, following the assumptions of the theory.

Note that Parez *et al.* [51] assume that the height of the flowing layer, h, as well as solids fraction ϕ remain constant and do not change with time. For this reason the time variation of the average solids fraction is not captured by their theory. We use the steady-state height h_s and solids fraction ϕ_s in Eq. (A1) to calculate the predictions shown in Fig. 21. DEM simulation results are shown using
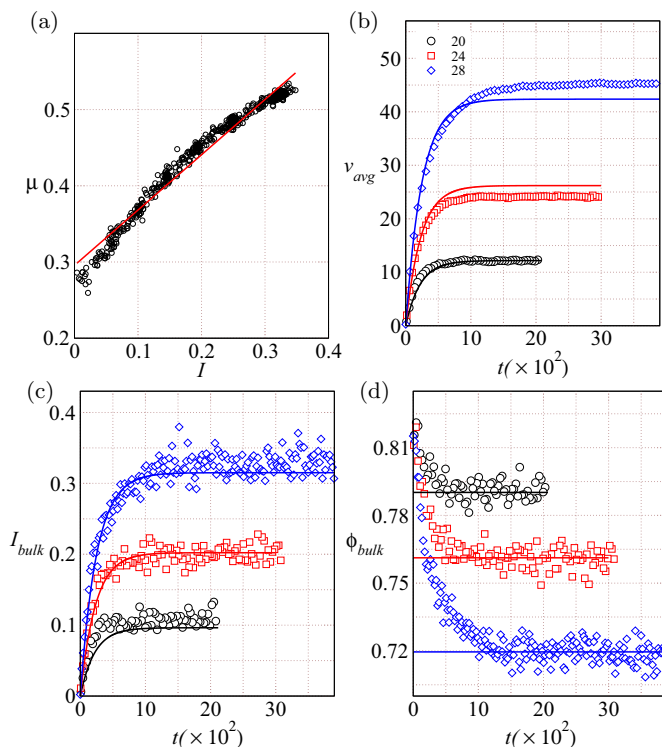
FIG. 21. (a) Variation of effective friction coefficient μ with inertial number I for restitution coefficient $e_n = 0.5$. Black circles represent the DEM data up to inclination $\theta = 28°$. The solid red line represents the fitted line of the form $\mu(I) = aI + b$. Variation of the (b) average velocity of the layer, v_{avg}, (c) average inertial number in the bulk, I_{bulk}, and (d) average solids fraction in the bulk, ϕ_{bulk}, with time t for $e_n = 0.5$ at different inclinations. Symbols represent the DEM simulation data and the solid lines represent the analytical predictions by Parez et al. [51].

symbols. The profiles predicted using their analytical solution are in reasonable agreement with the DEM data up to $I_{bulk} = 0.3$. At earlier times, the difference between theory and simulations is observable due to the difference in the μ-I data and the linear fit used. Fitting a line only for data lying in the range $I < 0.1$ improves the analytical predictions for $\theta = 20°$. Similarly, a better match can be obtained for $\theta = 24°$ by using a linear fit only up to $I \sim 0.2$.

At a higher inclination angle of $\theta = 28°$, the analytical predictions for v_{avg} differ from simulation data not only for early times but also for later times. Increasing the inclination angle further leads to more deviation from the simulation data since the nonlinear behavior of the data is not captured well using a linear fit for higher values of the inertial number observed at these high inclinations. In the absence of any theoretical results for nonlinear μ-I relation, we resort to the numerical solution of the momentum balance equations in the next sections. Before reporting the numerical results of momentum balance equations for the nonlinear μ-I rheology, we compare our numerical predictions for the linear μ-I case with the analytical solutions of Parez et al. [51]. We first benchmark our numerical solutions using the rheological parameters reported by Parez et al. [51] and find a near-perfect match with their analytical solutions (not shown here). Next, we use the fitted parameter for the linear μ-I relation from Fig. 21(a) to obtain numerical solutions corresponding to the analytical solutions shown in Fig. 21(b). Figure 22(a) shows the results for the velocity profile at different time instants for $\theta = 24°$. Figure 22(b) shows the average velocity v_{avg} variation with time for three different inclinations. The dashed line corresponds to the single-term solution while the solid
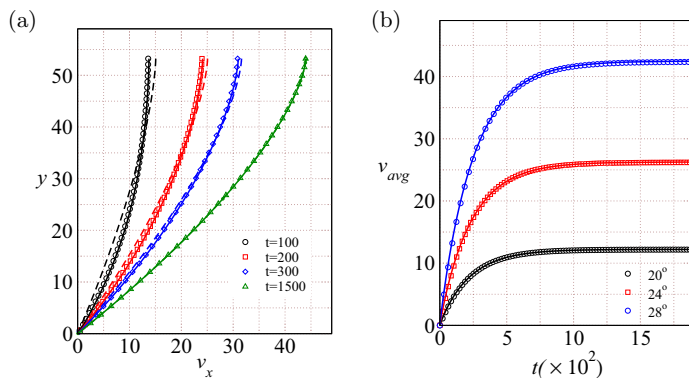
FIG. 22. (a) Comparison of the numerical solution (shown using symbols), analytical one-term solution (dashed line), and analytical three-term solution (solid lines) at different times for $\theta = 24°$. (b) Comparison of the numerical solution (shown using symbols) and analytical one-term solution (solid lines) for different angles.

line accounts for the first three terms of the infinite series solution. The slight difference between the single-term solution and the three-term solution is due to the fact that the neglected terms of the series solution remain comparable to the first term of the series at smaller times and become negligible only at large times. In the next sections, we use this numerical method with nonlinear μ-I relation to obtain predictions for the flow properties with time. The excellent match between the numerical solutions (symbols) and analytical predictions (solid lines) confirms the accuracy of the numerical solutions.

APPENDIX B: NORMAL STRESS PROFILES AT DIFFERENT TIMES

Figures 23(a)–23(c) show the variation of the normal stresses σ_{yy}, σ_{xx} and pressure P with the distance from the base y for inclination angle $\theta = 28°$ at different times t corresponding to the restitution coefficient $e_n = 0.5$. The results suggested that a linear variation of the normal stresses σ_{yy}, σ_{xx} and pressure P is observed with the distance from the base y and is found to be a maximum

FIG. 23. Variation of the (a) normal stress σ_{yy}, (b) normal stress σ_{xx}, and (c) pressure P with distance y from the base at different times for $\theta = 28°$. Symbols represent the DEM simulation data ($e_n = 0.5$) and solid lines are the predictions of the modified rheology.
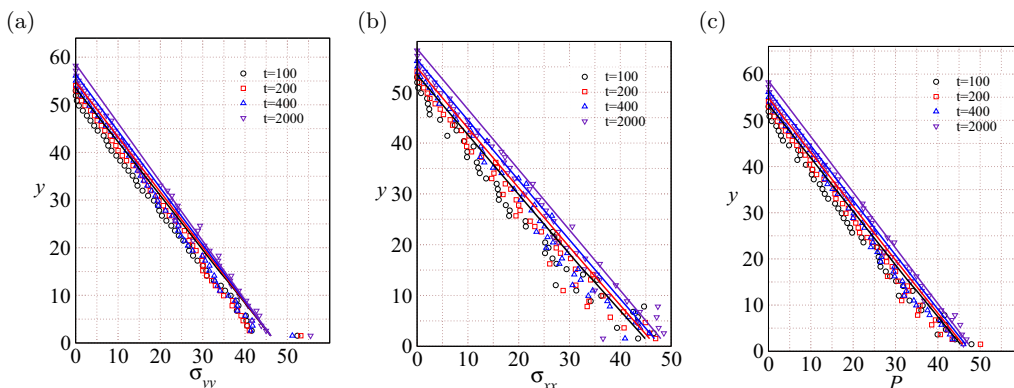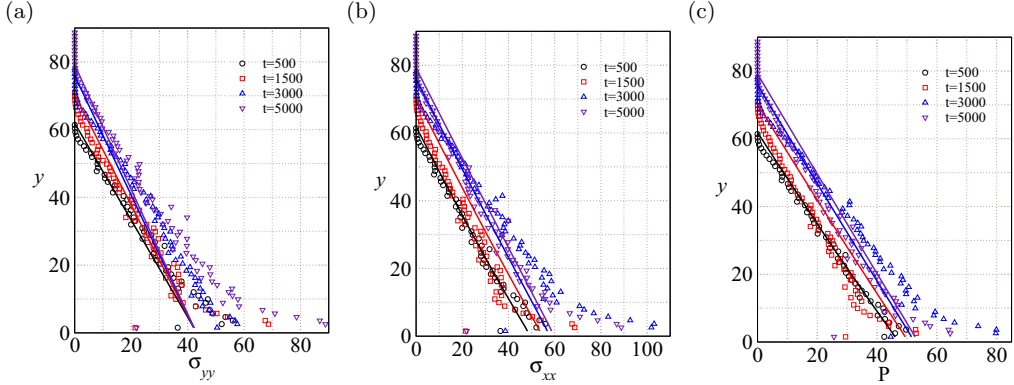
FIG. 24. Variation of the (a) normal stress σ_{yy}, (b) normal stress σ_{xx}, and (c) pressure P with distance y from the base at different times for $\theta = 36°$. Symbols represent the DEM simulation data ($e_n = 0.5$) and solid lines are the predictions of the modified rheology.

at the base $y = 0$. The theoretical predictions using the modified rheological model (shown using solid lines) are able to capture the DEM simulation data (shown using symbols) reasonably well.

In Figs. 24(a)–24(c), we show the variation of the normal stresses σ_{yy}, σ_{xx} and pressure P with the distance from the base y for inclination angle $\theta = 36°$ at different times t corresponding to the restitution coefficient $e_n = 0.5$. Figure 24(a) shows the variation of the normal stress σ_{yy} with the distance from the base y. The DEM data show that the σ_{yy} at early times is well predicted by the theory for most of the layer except in the region near the base. The theoretical predictions are found to be smaller than the values observed in DEM simulations near the base region. As the time increases, the region of the discrepancy between the simulations and theory increases. While the vertical stress in the DEM keeps increasing near the base with time, the theoretically predicted value of σ_{yy} at the base remains the same. This can be understood as follows. σ_{yy} shows a linear dependence with the depth because of the constant solids fraction ϕ at any instant as per Eq. (4). As per Eq. (4), the height h will change with time t as per the dilatancy law [Eq. (9)] and mass balance (as per line 18 of Algorithm 1). Evidently, this increased height with time is captured well by the theory. However, the value of σ_{yy} at the base (i.e., at $y = 0$) according to Eq. (4) remains equal to $\rho_p g h \cos \theta$ at all times (since $h\phi_{\mathrm{avg}}$ is constant) and gives a measure of the total weight of the granular bed in the normal direction. This discrepancy between the theory and DEM data arises due to the assumptions of steady, unidirectional flows in the theory. As reported in Sec. V C, the flow at higher inclinations is observed to be oscillatory in nature. Hence the existence of v_y and its variation with time need not be neglected. The theory ignores the presence of time-dependent v_y in the y component of the momentum balance equation [Eq. (2)], and fails to account for the effect of additional terms that govern the evolution of σ_{yy}. This discrepancy in σ_{yy} further leads to the discrepancies in P [by Eq. (11)] calculation as well, which in turn manifests in the calculation of σ_{xx} as well. Note that the theory predicts a similar linear variation of the σ_{xx} [Fig. 24(b)] and the pressure P [Fig. 24(c)] with y. Thus we conclude that the discrepancy in the theoretical predictions and the DEM simulation results for the pressure and normal stresses at later times can be attributed to the oscillatory nature of the flow which leads to variations in the layer height and significant slip velocity at the base, along with a low-density region near the base.

APPENDIX C: OSCILLATIONS AT HIGH INCLINATIONS

Reference [77] shows the video of the flow for inclination angles $\theta = 24°$ and $\theta = 36°$. In order to highlight the oscillations in the granular bed height, a black line is shown at the y location of the particle having maximum height. No such surface exists in the DEM simulations and the top surface

of the simulation box is kept significantly away from maximum y location of the particles to ensure that the motion of the particles does not experience its presence. Evidently, the entire layer oscillates vigorously at $\theta = 36°$. These oscillations correspond to the dominant frequency $f \sim 0.043$ as seen in Fig. 19 which is equivalent to 4.3 Hz for 1-mm particles. In contrast, the $\theta = 24°$ case does not show significant oscillations.

[1] O. Pouliquen, Scaling laws in granular flows down rough inclined planes, Phys. Fluids **11**, 542 (1999).

[2] G. MiDi, On dense granular flows., Eur. Phys. J. E **14**, 341 (2004).

[3] P. Jop, Y. Forterre, and O. Pouliquen, Crucial role of sidewalls in granular surface flows: Consequences for the rheology, J. Fluid Mech. **541**, 167 (2005).

[4] A. J. Holyoake and J. N. McElwaine, High-speed granular chute flows, J. Fluid Mech. **710**, 35 (2012).

[5] O. Pouliquen, On the shape of granular fronts down rough inclined planes, Phys. Fluids **11**, 1956 (1999).

[6] J. Heyman, P. Boltenhagen, R. Delannay, and A. Valance, Experimental investigation of high speed granular flows down inclines, EPJ Web Conf. **140**, 03057 (2017).

[7] E. L. Thompson and H. E. Huppert, Granular column collapses: Further experimental results, J. Fluid Mech. **575**, 177 (2007).

[8] L. Lacaze, J. C. Phillips, and R. R. Kerswell, Planar collapse of a granular column: Experiments and discrete element simulations, Phys. Fluids **20**, 063302 (2008).

[9] G. Lube, H. E. Huppert, R. S. J. Sparks, and M. A. Hallworth, Axisymmetric collapses of granular columns, J. Fluid Mech. **508**, 175 (2004).

[10] E. Lajeunesse, A. Mangeney-Castelnau, and J. Vilotte, Spreading of a granular mass on a horizontal plane, Phys. Fluids **16**, 2371 (2004).

[11] Y. Zhou, P.-Y. Lagrée, S. Popinet, P. Ruyer, and P. Aussillous, Experiments on, and discrete and continuum simulations of, the discharge of granular media from silos with a lateral orifice, J. Fluid Mech. **829**, 459 (2017).

[12] D. Khakhar, J. McCarthy, and J. M. Ottino, Radial segregation of granular mixtures in rotating cylinders, Phys. Fluids **9**, 3600 (1997).

[13] S. Ji, D. M. Hanes, and H. H. Shen, Comparisons of physical experiment and discrete element simulations of sheared granular materials in an annular shear cell, Mech. Mater. **41**, 764 (2009).

[14] E. Azanza, F. Chevoir, and P. Moucheront, Experimental study of collisional granular flows down an inclined plane, J. Fluid Mech. **400**, 199 (1999).

[15] S.-C. Yang and S.-S. Hsiau, The simulation and experimental study of granular materials discharged from a silo with the placement of inserts, Powder Technol. **120**, 244 (2001).

[16] A. V. Orpe and D. Khakhar, Rheology of surface granular flows, J. Fluid Mech. **571**, 1 (2007).

[17] M. I. Arran, A. Mangeney, J. De Rosny, M. Farin, R. Toussaint, and O. Roche, Laboratory landquakes: Insights from experiments into the high-frequency seismic signal generated by geophysical granular flows, J. Geophys. Res.: Earth Surf. **126**, e2021JF006172 (2021).

[18] V. Bachelet, A. Mangeney, R. Toussaint, J. de Rosny, M. I. Arran, M. Farin, and C. Hibert, Acoustic emissions of nearly steady and uniform granular flows: A proxy for flow dynamics and velocity fluctuations, J. Geophys. Res.: Earth Surf. **128**, e2022JF006990 (2023).

[19] L. E. Silbert, D. Ertaş, G. S. Grest, T. C. Halsey, D. Levine, and S. J. Plimpton, Granular flow down an inclined plane: Bagnold scaling and rheology, Phys. Rev. E **64**, 051302 (2001).

[20] F. da Cruz, S. Emam, M. Prochnow, J.-N. Roux, and F. Chevoir, Rheophysics of dense granular materials: Discrete simulation of plane shear flows, Phys. Rev. E **72**, 021309 (2005).

[21] O. Pouliquen, C. Cassar, P. Jop, Y. Forterre, and M. Nicolas, Flow of dense granular material: Towards simple constitutive laws, J. Stat. Mech. (2006) P07020.

[22] O. Baran, D. Ertaş, T. C. Halsey, G. S. Grest, and J. B. Lechman, Velocity correlations in dense gravity-driven granular chute flow, Phys. Rev. E **74**, 051302 (2006).

[23] T. Börzsönyi, R. E. Ecke, and J. N. McElwaine, Patterns in flowing sand: Understanding the physics of granular flow, Phys. Rev. Lett. **103**, 178302 (2009).

[24] A. Tripathi and D. Khakhar, Rheology of binary granular mixtures in the dense flow regime, Phys. Fluids **23**, 113302 (2011).

[25] V. Kumaran and S. Bharathraj, The effect of base roughness on the development of a dense granular flow down an inclined plane, Phys. Fluids **25**, 070604 (2013).

[26] N. Brodu, R. Delannay, A. Valance, and P. Richard, New patterns in high-speed granular flows, J. Fluid Mech. **769**, 218 (2015).

[27] S. Mandal and D. V. Khakhar, A study of the rheology of planar granular flow of dumbbells using discrete element method simulations, Phys. Fluids **28**, 103301 (2016).

[28] V. J.-L. Ralaiarisoa, A. Valance, N. Brodu, and R. Delannay, High speed confined granular flows down inclined: Numerical simulations, EPJ Web Conf. **140**, 03081 (2017).

[29] S. Mandal and D. Khakhar, A study of the rheology and micro-structure of dumbbells in shear geometries, Phys. Fluids **30**, 013303 (2018).

[30] A. Bhateja and D. V. Khakhar, Rheology of dense granular flows in two dimensions: Comparison of fully two-dimensional flows to unidirectional shear flow, Phys. Rev. Fluids **3**, 062301(R) (2018).

[31] A. Bhateja and D. V. Khakhar, Analysis of granular rheology in a quasi-two-dimensional slow flow by means of discrete element method based simulations, Phys. Fluids **32**, 013301 (2020).

[32] S. Patro, M. Prasad, A. Tripathi, P. Kumar, and A. Tripathi, Rheology of two-dimensional granular chute flows at high inertial numbers, Phys. Fluids **33**, 113321 (2021).

[33] B. Debnath, K. K. Rao, and V. Kumaran, Different shear regimes in the dense granular flow in a vertical channel, J. Fluid Mech. **945**, A25 (2022).

[34] Y. Forterre and O. Pouliquen, Flows of dense granular media, Annu. Rev. Fluid Mech. **40**, 1 (2008).

[35] Y. F. B. Andreotti and O. Pouliquen, *Granular Media: Between Fluid and Solid* (Cambridge University Press, Cambridge, UK, 2013).

[36] P. Jop, Rheological properties of dense granular flows, C. R. Phys. **16**, 62 (2015).

[37] P. Jop, Y. Forterre, and O. Pouliquen, A constitutive law for dense granular flows, Nature (London) **441**, 727 (2006).

[38] P.-Y. Lagrée, L. Staron, and S. Popinet, The granular column collapse as a continuum: Validity of a two-dimensional Navier-Stokes model with a $\mu(I)$ rheology, J. Fluid Mech. **686**, 378 (2011).

[39] M. Renouf, D. Bonamy, F. Dubois, and P. Alart, Numerical simulation of two-dimensional steady granular flows in rotating drum: On surface flow rheology, Phys. Fluids **17**, 103303 (2005).

[40] Y. Forterre and O. Pouliquen, Long-surface-wave instability in dense granular flows, J. Fluid Mech. **486**, 21 (2003).

[41] S. Mandal and D. V. Khakhar, Sidewall-friction-driven ordering transition in granular channel flows: Implications for granular rheology, Phys. Rev. E **96**, 050901(R) (2017).

[42] K. Kamrin, Nonlinear elasto-plastic model for dense granular flow, Int. J. Plast. **26**, 167 (2010).

[43] T. Barker and J. M. N. T. Gray, Partial regularisation of the incompressible $\mu(I)$ rheology for granular flow, J. Fluid Mech. **828**, 5 (2017).

[44] T. Barker, M. Rauter, E. S. F. Maguire, C. G. Johnson, and J. M. N. T. Gray, Coupling rheology and segregation in granular flows, J. Fluid Mech. **909**, A22 (2021).

[45] C.-C. Lin and F.-L. Yang, Continuum simulation for regularized non-local $\mu(I)$ model of dense granular flows, J. Comput. Phys. **420**, 109708 (2020).

[46] J. Chauchat and M. Médale, A three-dimensional numerical model for dense granular flows based on the $\mu(I)$ rheology, J. Comput. Phys. **256**, 696 (2014).

[47] D. L. Henann and K. Kamrin, A predictive, size-dependent continuum model for dense granular flows, Proc. Natl. Acad. Sci. USA **110**, 6730 (2013).

[48] T. Barker, D. Schaeffer, P. Bohorquez, and J. Gray, Well-posed and ill-posed behaviour of the $\mu(I)$ rheology for granular flow, J. Fluid Mech. **779**, 794 (2015).

[49] S. Dunatunga and K. Kamrin, Continuum modelling and simulation of granular flows through their many phases, J. Fluid Mech. **779**, 483 (2015).

[50] A. Franci and M. Cremonesi, 3D regularized μ(I) rheology for granular flows simulation, J. Comput. Phys. **378**, 257 (2019).

[51] S. Parez, E. Aharonov, and R. Toussaint, Unsteady granular flows down an inclined plane, Phys. Rev. E **93**, 042902 (2016).

[52] L. Staron, P.-Y. Lagrée, and S. Popinet, The granular silo as a continuum plastic flow: The hour-glass vs the clepsydra, Phys. Fluids **24**, 103301 (2012).

[53] L. Staron, P.-Y. Lagrée, and S. Popinet, Continuum simulation of the discharge of the granular silo, Eur. Phys. J. E **37**, 5 (2014).

[54] M. Rauter, The compressible granular collapse in a fluid as a continuum: Validity of a Navier-Stokes model with μ(J), ϕ(J) rheology, J. Fluid Mech. **915**, A87 (2021).

[55] H. Xiao, J. M. Ottino, R. M. Lueptow, and P. B. Umbanhowar, Transient response in granular quasi-two-dimensional bounded heap flow, Phys. Rev. E **96**, 040902(R) (2017).

[56] M. Pilvar, M. J. Pouraghniaei, and A. Shakibaeinia, Two-dimensional sub-aerial, submerged, and transitional granular slides, Phys. Fluids **31**, 113303 (2019).

[57] J. Gray and A. Edwards, A depth-averaged-rheology for shallow granular free-surface flows, J. Fluid Mech. **755**, 503 (2014).

[58] F. Rocha, C. Johnson, and J. Gray, Self-channelisation and levee formation in monodisperse granular flows, J. Fluid Mech. **876**, 591 (2019).

[59] R. Delannay, A. Valance, A. Mangeney, O. Roche, and P. Richard, Granular and particle-laden flows: From laboratory experiments to field observations, J. Phys. D **50**, 053001 (2017).

[60] A. Mangeney, F. Bouchut, N. Thomas, J.-P. Vilotte, and M.-O. Bristeau, Numerical modeling of self-channeling granular flows and of their levee-channel deposits, J. Geophys. Res.: Earth Surf. **112**, 2006JF000469 (2007).

[61] P. V. Dsouza and P. R. Nott, A non-local constitutive model for slow granular flow that incorporates dilatancy, J. Fluid Mech. **888**, R3 (2020).

[62] O. Pouliquen and Y. Forterre, A non-local rheology for dense granular flows, Philos. Trans. R. Soc. A **367**, 5091 (2009).

[63] K. Kamrin and G. Koval, Nonlocal constitutive relation for steady granular flow, Phys. Rev. Lett. **108**, 178301 (2012).

[64] M. Bouzid, A. Izzet, M. Trulsson, E. Clément, P. Claudin, and B. Andreotti, Non-local rheology in dense granular flows: Revisiting the concept of fluidity, Eur. Phys. J. E **38**, 125 (2015).

[65] B. Debnath, V. Kumaran, and K. K. Rao, Comparison of the compressible μ(I) class of models and non-local models with the discrete element method for steady fully developed flow of cohesionless granular materials through a vertical channel, J. Fluid Mech. **937**, A33 (2022).

[66] T. Barker, D. G. Schaeffer, M. Shearer, and J. M. N. T. Gray, Well-posed continuum equations for granular flow with compressibility and μ(I) rheology, Proc. R. Soc. A **473**, 20160846 (2017).

[67] D. Schaeffer, T. Barker, D. Tsuji, P. Gremaud, M. Shearer, and J. Gray, Constitutive relations for compressible granular flow in the inertial regime, J. Fluid Mech. **874**, 926 (2019).

[68] K. Kamrin, Non-locality in granular flow: Phenomenology and modeling approaches, Front. Phys. **7**, 116 (2019).

[69] J. Heyman, R. Delannay, H. Tabuteau, and A. Valance, Compressibility regularizes the μ(I) rheology for dense granular flows, J. Fluid Mech. **830**, 553 (2017).

[70] I. Goldhirsch and N. Sela, Origin of normal stress differences in rapid granular flows, Phys. Rev. E **54**, 4458 (1996).

[71] M. Alam and S. Luding, First normal stress difference and crystallization in a dense sheared granular fluid, Phys. Fluids **15**, 2298 (2003).

[72] S. Saha and M. Alam, Normal stress differences, their origin and constitutive relations for a sheared granular fluid, J. Fluid Mech. **795**, 549 (2016).

[73] I. Srivastava, L. E. Silbert, G. S. Grest, and J. B. Lechman, Viscometric flow of dense granular materials under controlled pressure and shear stress, J. Fluid Mech. **907**, A18 (2021).

[74] A. P. Santos, I. Srivastava, L. E. Silbert, J. B. Lechman, and G. S. Grest, Fluctuations and power-law scaling of dry, frictionless granular rheology near the hard-particle limit, Phys. Rev. Fluids **7**, 084303 (2022).

[75] S. Athani, B. Metzger, Y. Forterre, and R. Mari, Transient flows and migration in granular suspensions: Key role of Reynolds-like dilatancy, J. Fluid Mech. **949**, A9 (2022).

[76] S. Savage, Instability of unbounded uniform granular shear flow, J. Fluid Mech. **241**, 109 (1992).

[77] https://youtube.com/playlist?list=PLzCaWi491edy-PKVOP0Yl3s8GtSTgEkcq.

[78] C.-H. Wang, R. Jackson, and S. Sundaresan, Stability of bounded rapid shear flows of a granular material, J. Fluid Mech. **308**, 31 (1996).

[79] Y. Forterre and O. Pouliquen, Stability analysis of rapid granular chute flows: Formation of longitudinal vortices, J. Fluid Mech. **467**, 361 (2002).

[80] R. B. Bird, W. E. Stewart, and E. N. Lightfoot, *Transport Phenomena, 2nd Edition* (John Wiley & Sons, New York, 2007).

[81] M. Louge, A. Valance, N. Taberlet, P. Richard, and R. Delannay, Volume fraction profile in channeled granular flows down an erodible incline, Proc. Powders Grains **2**, 885 (2005).

[82] Z. Shojaaee, J.-N. Roux, F. Chevoir, and D. E. Wolf, Shear flow of dense granular materials near smooth walls. I. Shear localization and constitutive laws in the boundary region, Phys. Rev. E **86**, 011301 (2012).